

# **COMPARISON OF THE UPDATED SOLUTIONS OF THE 6<sup>TH</sup> DYNAMIC AER BENCHMARK – MAIN STEAM LINE BREAK IN A NPP WITH VVER-440**

S. Kliem  
Forschungszentrum Rossendorf  
Institute of Safety Research  
P.O.B. 51 01 19, D-01314 Dresden, Germany

## **ABSTRACT**

The 6<sup>th</sup> dynamic AER Benchmark is used for the systematic validation of coupled 3D neutron kinetic/thermal hydraulic system codes. It was defined at the 10<sup>th</sup> AER-Symposium. In this benchmark, a hypothetical double ended break of one main steam line at full power in a VVER-440 plant is investigated. The main thermal hydraulic features are the consideration of incomplete coolant mixing in the lower and upper plenum of the reactor pressure vessel and an asymmetric operation of the feed water system. For the tuning of the different nuclear cross section data used by the participants, an isothermal re-criticality temperature was defined.

First solutions of the benchmark were compared during the 11<sup>th</sup> AER-Symposium. Due to the considerable spreading of these first results, the participants continued the work on the calculation of the benchmark. Updated solutions were received from VTT Processes Espoo (HEXTRAN/SMABRE), Kurchatov Institute Moscow (BIPR8/ATHLET), NRI Rez (RELAP5-3D) and Forschungszentrum Rossendorf (DYN3D/ATHLET). The solution of KFKI AEKI Budapest (KIKO3D/ATLET) remained unchanged.

The paper gives an overview on the behaviour of the main thermal hydraulic and neutron kinetic parameters in the provided solutions. The differences in the updated solution in comparison to the previous ones are described. Improvements in the modelling of the transient led to a better agreement of a part of the results while for another part the deviations rose up. The sensitivity of the core power behaviour on the secondary side modelling is discussed in detail.

## 1. INTRODUCTION

The fifth dynamic AER benchmark was the first benchmark for coupled 3D hexagonal neutron kinetic core models/thermohydraulic system codes. Definition and comparison of solutions have been published in the proceedings of the 7<sup>th</sup> and 8<sup>th</sup> AER symposium [1, 2]. In that benchmark, considering a main steam header break at a subcritical reactor, some simplifications are made to reduce the complexity of the calculation.

The sixth dynamic AER benchmark [3] is the continuation of a systematic validation of coupled 3D neutron kinetic/thermohydraulic system codes. A number of features not considered in the fifth dynamic benchmark are present in the current one. This concerns an asymmetrical leak (break of one main steam line) and the consideration of coolant mixing in the upper and the lower plenum of the reactor pressure vessel. Further, an asymmetrical feed water behaviour is considered. The different nuclear data used by the participants are normalized by defining a recriticality temperature.

Solutions were compared during the 11<sup>th</sup> AER-Symposium [4]. A considerable spreading of the results was observed. Further, not all participants followed fully the benchmark specification. So, it was decided to continue the work on the calculation of the benchmark.

Improvements in single solutions were reported at the working group D meeting in 2002. The current paper presents the final comparison of the solutions of the benchmark.

Tab. 1 gives an overview on the participants in the calculations of the 6<sup>th</sup> Dynamic AER Benchmark. The neutron kinetic core models and thermal hydraulic system codes used for the calculations are included into the table. The last two columns show the date of the submission of the first and the updated solution.

Tab. 1: Overview on the participants of the benchmark calculations

<b>Organization</b>	<b>Country</b>	<b>3D Neutron kinetics core model</b>	<b>Thermohydraulics system code</b>	<b>First solution</b>	<b>update</b>
Kurchatov Institute	Russia	BIPR8	ATHLET	May, 2001	May, 2002
VTT Processes	Finland	HEXTRAN	SMABRE	May, 2001	August, 2003
NRI Rez	Czech Republic	NESTLE	RELAP5-3D	May, 2001	September, 2003
KFKI Budapest	Hungary	KIKO3D	ATHLET	July, 2001	-
FZ Rossendorf	Germany	DYN3D	ATHLET	May, 2001	May, 2002

## 2. COMPARISON OF THE KEY PARAMETERS

Tab. 2 gives an overview on the events in the different calculations.

Tab. 2: Table of events (time in s)

Event	FZR	VTT	AEKI	NRI	KI
Leak opening	0.0	0.0	0.0	0.0	0.0
Start 1 <sup>st</sup> make-up pump	13.4	3.1	5.6	7.5	
SCRAM value reached	19.5	11.1	13.9	14.2	39.9
PRZ Heater group 1 on	20.3	5.8	7.6		28.2
PRZ Heater group 2 on	24.5	7.3	13.9	9.0	30.7
PRZ Heater group 3 on	27.0	8.8	17.3	16.0	33.8
PRZ Heater group 4 on	31.5	14.0	22.4	22.5	47.6
PRZ Heater groups off	51.5	5.27	51.3	66.5	
PRZ-Level <2.41m	54.1	55.9		69.0	71.3
HPIS Signal	54.1	55.9	54.2	69.5	71.3
Start 2 <sup>nd</sup> make-up pump	53.6		45.6	47.5	
Pressure in MSH <3.0MPa	89.0	55.9	64.4	99.5	98.7
Begin of HPIS supply	234.1	235.9	234.2	249.5	251.3
Second power maximum	272.0	253.0	225.8	234.5	256.5
End of calculation	400.0	398.0	400.0	1000.0	400.0

Tab. 3 contains the requested key parameters of the different calculations.

Tab. 3: Comparison of key parameters

Parameter		FZR	VTT	AEKI	NRI	KI
Total core power [MW]	T=0.0s	1351.0	1376.8	1374.4	1375.0	1375.0
	1 <sup>st</sup> power maximum	1521.4	1516.2	1503.5	1518.6	1532.3
	2 <sup>nd</sup> power maximum	43.5	58.3	130.3	209.8	87.1
Total fission power [MW]	T=0.0s	1265.0	1283.3	1278.5	1284.8	1278.5
	1 <sup>st</sup> power maximum	1433.0	1421.2	1405.8	1426.9	1436.5
	2 <sup>nd</sup> power maximum	10.3	18.5	98.7	163.1	48.7
3D power peak factor (FA;Layer)	T=0.0s	1.5164 (28;4)	1.5302 (36)	1.639 (183;3)	-	1.534 (28;3)
	1 <sup>st</sup> power maximum	1.5680 (183;4)	1.5567 (183)	1.683 (183;3)	-	2.683 (183;3)
	2 <sup>nd</sup> power maximum	10.6746 (222;10)	12.1425 (222)	11.947 (144;9)	-	10.194 (144;9)
Isothermal MTC	pcm/K	-35.1	-29.3	-29.8	-30.1	-41.3
CR worth before tuning	pcm	6583	5670	5397	5250	6612
CR worth after tuning	pcm	4228	3571	3571	3543	4155

### 3. COMPARISON OF THE DIFFERENT PHASES OF THE TRANSIENT

The transient can be divided into three parts. The opening of the leak causes a depressurization of the secondary side and a resulting overcooling of the primary circuit. The core power increases and activates the reactor scram. In the second phase (after reactor scram), the feeding of the steam generators continues until the main steam header pressure reaches the activation value for the closure of the main steam isolation valves and the closure of the feed water supply. In the last phase, the overcooling continues until the steam generator 1 is empty. The overcooling leads to a second power rise, which is stopped by the injection of highly-borated water from the high pressure injection system.

#### 3.1 FIRST PHASE (FROM LEAK OPENING UNTIL THE REACTOR SCRAM)

Fig. 1 and 2 show the time course of the total core power. After leak opening, the core power increases in all solutions. The power level of 110 %, necessary for the activation of the reactor scram is reached at different time points in the various solutions (see Tab. 1). First of all, the scram value is reached in the VTT-calculation, followed by the AEKI and the NRI-calculations within less than 3 s. The scram value in the FZR-calculation is reached about 5 s after the NRI-calculation. More than 20 s later, the scram value is reached in the KI-calculation.

The power increase after leak opening is determined by two factors, by the amount of overcooling and by the moderator temperature coefficient. The average core inlet temperature is shown in Fig. 3. The decrease of this average temperature from leak opening until reaching the scram value is in all calculations nearly the same. The different isothermal moderator coefficients, determined for a coolant temperature of 210 °C and inserted control rods, seem not to have a big influence onto the power behaviour until the reactor scram. That means, that the spreading of the time of reaching the scram value is caused by differences in the rate of overcooling. It can be clearly concluded from Fig. 3, that the higher the overcooling rate the faster the scram value is reached. The time delay for reaching the scram value in the KI-calculation is connected with the fact, that shortly after leak opening, the overcooling is stopped for a certain time, the average core inlet temperature rises again. Only after some 20 s the overcooling continues and the scram value is reached, what causes the reactor scram. The reason for such a different from the other calculations behaviour is in the secondary circuit, namely in the behaviour of the intact steam generators.

Fig. 5 shows the heat transfer summarized over all six steam generators. The higher the heat transfer from primary to secondary side, the higher is the overcooling. Three solutions show more or less the same behaviour, the VTT-calculation yields a higher level of about 20 %. The higher heat transfer in the VTT-calculation corresponds with the temperature curve (Fig. 3) and is also responsible for the fastest upper plenum pressure decrease (Fig. 4). In all mentioned calculations, the heat transfer rises until the scram. In the KI-calculation, already at  $t = 5\text{s}$ , the heat transfer starts to decrease.

The splitting of the heat transfer between the steam generator of the broken steam line and the remaining intact reveals, that this deviation in the summary heat transfer value in the KI-calculations comes from the behaviour of the intact steam generators (Figs. 5 and 6). The behaviour of the intact steam generator pressure in the single calculations (Fig. 21 and 22) is

in agreement with the observations in the time course of the heat transfer.

The leak mass flow rate is shown in Figs. 9 - 11. The explanation for a lower mass flow rate in the VTT-calculation can be seen in Figs. 12 and 13, where the leak steam and liquid mass flow rate are shown. Nearly no liquid is going through the leak in the VTT-calculation, while the other four calculations show a significant liquid mass flow rate through the leak until  $t = 30$  s. A very high amount of liquid is ejected in the KI-calculation, what could be the reason for the different pressure behaviour. The effect of different liquid entrainment is also reflected in the inventory of the broken steam generator (Fig. 33). The VTT-calculation shows the highest normalized inventory and KI the lowest.

### **3.2 SECOND PHASE (FROM REACTOR SCRAM UNTIL ISOLATION OF THE STEAM GENERATORS)**

The reactor scram decreases the power generation in the core to the decay heat level. The heat transfer in the steam generators reduces in all calculations, too. In the intact steam generator, the heat transfer decreases to a level of about 100 MW during a time of 20 s after reactor scram in all calculations.

The reactor scram stops the pressure decrease in the intact steam generators in all calculations. After a short increase, the pressure drops until the isolation of the intact steam generators. The level in the intact steam generators (Fig. 24) remains nearly constant. That is due to the working level control system in these steam generators. The reactor scram does not influence the pressure behaviour in the steam generator of the broken line in all calculations. The decrease continues smoothly during the whole time interval (Fig. 20). The level in the broken steam generator (Fig. 23) shows nearly the same behaviour in all calculations (considering the “Riser”-value of the VTT-calculation). The overfeeding during a short time interval before the steam generator isolation is reflected in a level increase during this time in all calculations. This can be seen also in the normalized steam generator inventory, shown in Fig. 33. After the reactor scram, the feed water injection in all calculations is higher than the leak flow rate, what expresses in a rising inventory.

When the main steam header pressure (Figs. 31, 32) decreases down to a value of 3.0 MPa, the main steam isolation valves and the feed water valves are closed. In such a way, five steam generators will be fully isolated. Due to the leak position, the steam generator of the steam line with the leak cannot be isolated and this steam generator continues to loss its inventory until fully depressurization. As can be seen from Figs. 31 and 32, the main steam header pressure decreases during the first phase of the transient in all calculations. After scram, the pressure increases for a short time period, in the KI-calculation already before the reactor scram. Later, the pressure decreases nearly with the same gradient in all calculations. Due to the differences in the maximum value reached after scram, a considerable spreading in the time of reaching the set point of steam generator isolation (3.0 MPa) is observed. According to Tab. 2, this spreading is from  $t = 55.9$  s (VTT) to  $t = 99.5$  s (KI). The isolation of the steam generators stops the heat transfer in the intact steam generators (Fig. 6).

### 3.3 THIRD PHASE (FROM ISOLATION OF THE STEAMGENERATORS)

After the isolation of the intact steam generators, the overcooling continues only in the steam generator of the broken line. The further decrease of the cold leg temperature of the intact loops is connected only with the coolant mixing in the lower and upper plenum. The decreasing level and inventory of the broken steam generator lead to an aggravation of the heat transfer conditions. At a certain level, the heat transfer tubes are no more covered by water and the heat transfer is almost fully stopped. This is the case at about  $t = 180$  s in the NRI- and AEKI-calculations. The others follow later.

During that time, the core power begins to rise in all calculations (Figs. 1 and 2). The power increase in the AEKI- and the NRI-calculations starts earlier. In these calculations maximum values of more than 100 MW are reached (130.3 MW - AEKI and 209.8 MW - NRI). In the remaining three calculations, the maximum values are lower (FZR – 43.5 MW, KI – 87.1 MW and VTT – 58.3 MW). The dynamic reactivity was provided from three calculations (Fig. 34). In all three calculations, the increase of the reactivity after scram starts nearly from the same value. The differences in the core inlet temperature of the sector connected to the loop with the broken steam line (Fig. 25) are responsible for the differences in the reactivity behaviour. The lower temperature in the AEKI-calculation leads to a faster compensation of the scram reactivity and subsequently to a higher second power peak.

The maximum fuel temperature in the second power peak (Fig. 34) is the highest in the AEKI-calculation, although the highest secondary power peak is observed in the NRI-calculation. The reduced number of thermal hydraulic core channels, used in the NRI-calculations is mainly responsible for smoothing the influence of this effect onto the maximum fuel temperature.

## 4. COMPARISON OF POWER DISTRIBUTIONS

The normalized axial power distribution (radially averaged) was requested for the time points of first end second power maximum. Fig. 37 shows this distribution at the moment of first power maximum. All calculations show a typical full power distribution with a maximum in the lower part of the core. The agreement between the four provided solutions is good.

After the scram and during the overcooling, a redistribution of the core power can be observed in all calculations. The maximum of the core power in the moment of second power maximum (Fig. 38) moves from the lower to the upper part of the core in all calculations. At this time point, the differences between the single calculations are higher. In the VTT-, FZR- and AEKI-calculations, the maximum of the normalized power distribution is nearly 1.5 or higher. In the KI-calculation, the power distribution is more flat, the maximum value is only about 1.2.

The 3D power peaking factor for three time points (initial state and the two time points of maximum core power) is provided in Tab. 3. In the initial state, the values of the single calculations are similar. At the moment of first power maximum, the value of the KI-calculation already deviates (probably due to the late time). At the moment of second power maximum, the differences are small. The position of the maximum is the neighbouring

assembly to the stuck rod K4 (VTT, AEKI) or neighbouring assembly to stuck rod K3 (FZR, KI).

The normalized 2D power distribution at the moment of second power maximum is shown in Figs. 39 – 42 for four calculation. The superposition of stuck control rods with the highest overcooling at the core inlet is clearly to be seen in the distributions of all four calculations. It seems, that in the KI-results the decay heat is included, therefore the normalized distribution differs slightly from the remaining ones.

## **5. INFLUENCE OF THE SECONDARY CIRCUIT MODELLING ON THE RESULTS**

As the first example, the influence of changes in the secondary side modelling on the behaviour of the main results is shown in Figs. 43 – 46 for the FZR-calculations. The two shown calculations differ only by the modelling of the connection between steam generator outlet and main steam line inlet. In the first calculation (FZR-old), the connection was realized as one pipe. The cross section of this pipe corresponded to the value at the real plant. Later, the modelling of this connection was improved, replacing this one pipe by five pipes with the original diameter. The flow area is equivalent between the two calculations. The reduced diameter in the new calculation is responsible for the lower leak liquid mass flow rate (Fig. 43), because the liquid entrainment is lower. This results in a smaller pressure decrease (Fig. 44), what reduces the heat transfer to the secondary side (Fig. 45) and the corresponding overcooling of the primary circuit. Due to that, the scram value is reached several seconds later and the second power maximum reaches a lower value (Fig. 46).

During the work on the benchmark, in the Kurchatov Institute a completely new steam generator model was developed and included into the ATHLET data set. The updated solution was obtained with this new steam generator model. As described in [5], the new steam generator model consists of different parts, allowing the modelling of an internal circulation. The separator model was also improved. The influence of the new steam generator model on the pressure behaviour is shown in Fig. 47. The pressure behaviour is responsible for the decreased overcooling during the first part of the transient and the corresponding delay of the reactor scram (Fig. 48).

## **6. CONCLUSIONS**

In this paper, the comparison of the updated solutions of the sixth dynamic AER benchmark is presented. Five solutions from five different organizations are included into this comparison.

A second power rise after the scram and the continuing overcooling of the primary circuit is observed in all calculations. Differences in the amount of overcooling result in a scattering of the height of this second power rise. Differences in the behaviour of the thermal hydraulic

parameters on the secondary side (especially in the pressure) are responsible for this scattering. The tuning of the isothermal recriticality temperature to the given value minimized the influence of using different nuclear data.

The sixth AER benchmark contributes to the verification of coupled 3D neutron kinetic/thermal hydraulic system codes. The analysis of such a complex benchmark promotes the understanding of the interaction processes between neutron kinetics and thermal hydraulics. Different physical models and data can be compared.

The calculation of this benchmark demonstrates the importance of the thermal hydraulic modelling of the plant components and the influence of this modelling on the final results of such calculations.

## 7. REFERENCES

- [1] S. Kliem: “ Definition of the Fifth Dynamic AER Benchmark Problem – A Benchmark for Coupled Thermohydraulic System/ Three-Dimensional Hexagonal Neutron Kinetic Core Models“, Proc. 7<sup>th</sup> Symposium of AER, pp. 429-438 , KFKI Atomic Energy Research Institute, Budapest (1997)
- [2] S. Kliem: “Comparison of the Results of the Fifth Dynamic AER Benchmark - A Benchmark for Coupled Thermohydraulic System/3D Hexagonal Neutron Kinetic Core Models“, Proc. 8<sup>th</sup> Symposium of AER, pp. 429-469, KFKI Atomic Energy Research Institute, Budapest (1998)
- [3] S. Kliem, A. Seidel, U. Grundmann: “Definition of the 6<sup>th</sup> Dynamic AER Benchmark - Main Steam Line Break in a NPP with VVER-440“, Proc. 10<sup>th</sup> Symposium of AER, pp. 749-762, KFKI Atomic Energy Research Institute, Budapest (2000)
- [4] S. Kliem, A. Seidel: “Comparison of the results of the 6<sup>th</sup> Dynamic AER Benchmark - Main Steam Line Break in a NPP with VVER-440 “, Proc. 11<sup>th</sup> Symposium of AER, pp. 295-329, KFKI Atomic Energy Research Institute, Budapest (2001)
- [5] S. Danilin, M. Lizorkin, S. Nikonov: “The new solution of the AER sixth benchmark problem with ATHLET/BIPR8KN code package “, Proc. 12<sup>th</sup> Symposium of AER, pp. 333-348, KFKI Atomic Energy Research Institute, Budapest (2002)

### 6. Dynamic AER Benchmark (update)

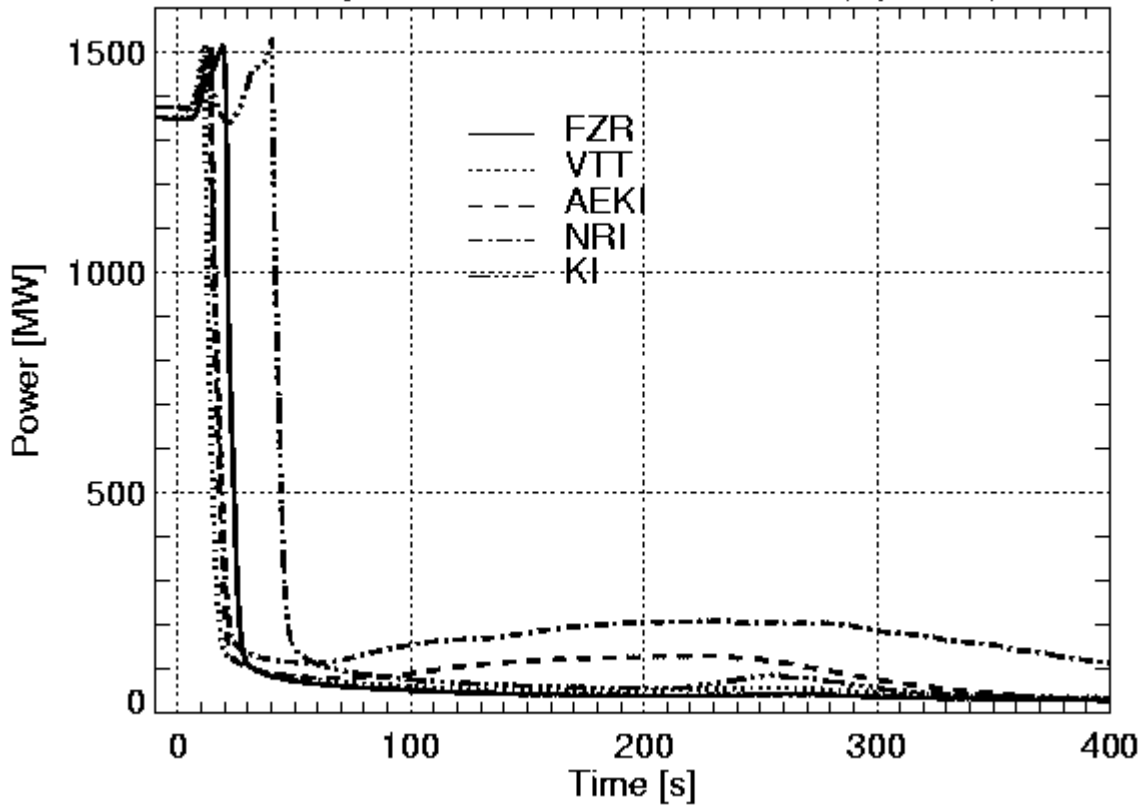


Fig. 1 Total core power

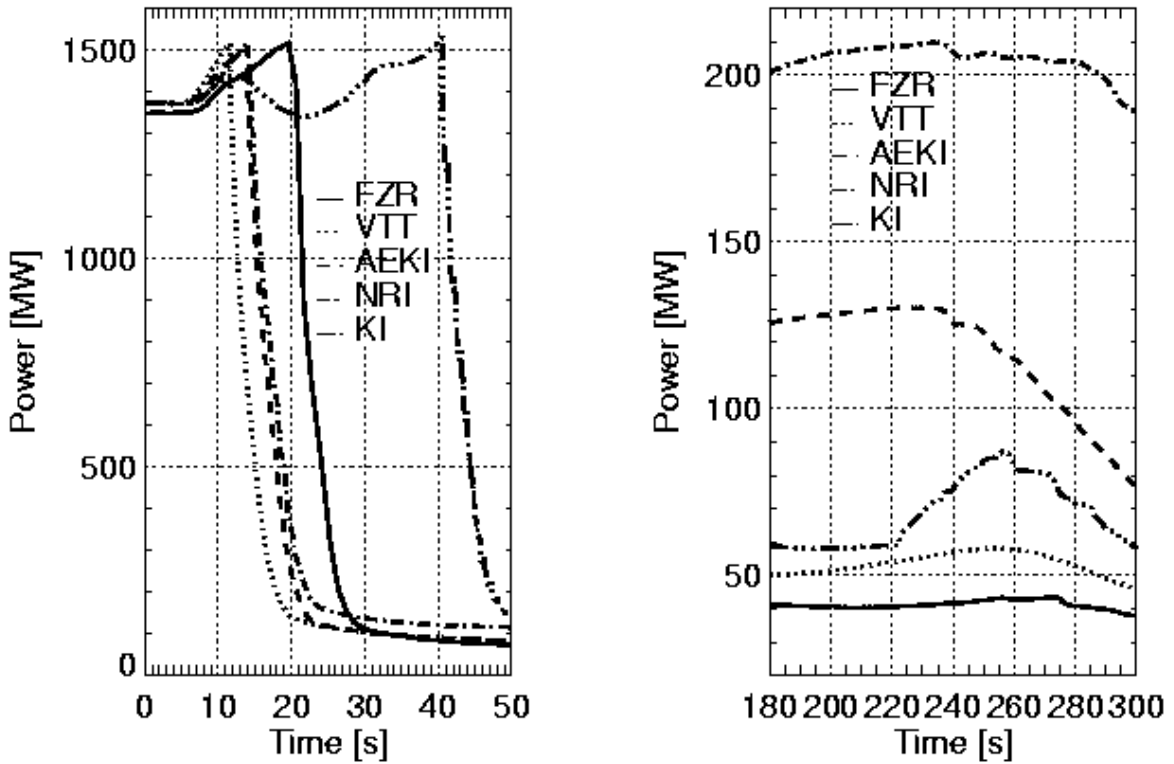


Fig. 2 Total core power (zoom)

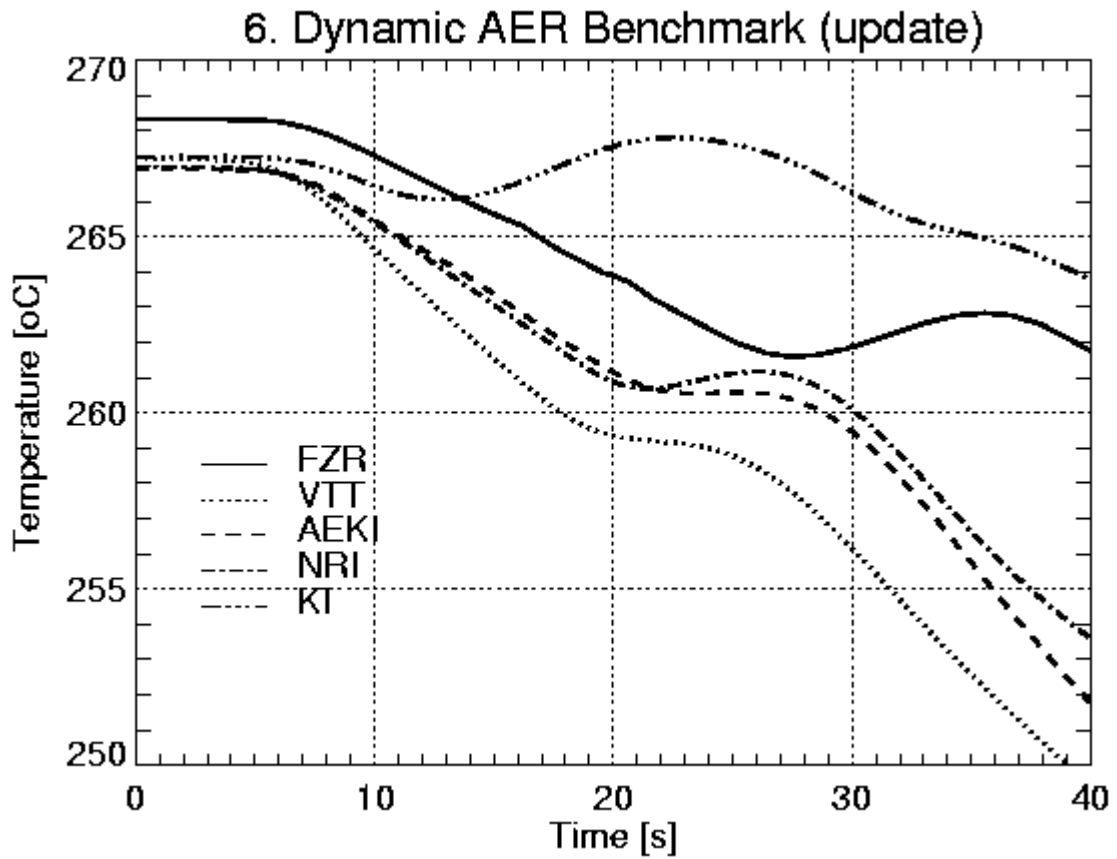


Fig. 3 Average core inlet temperature

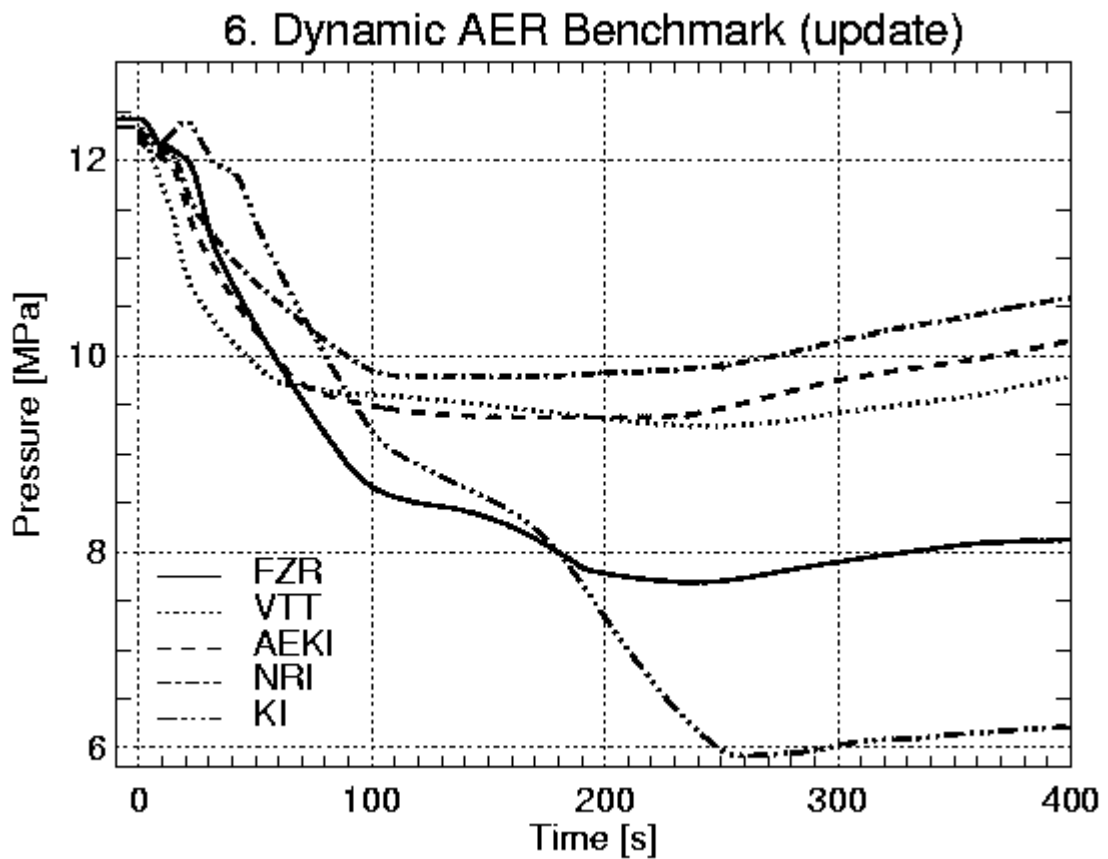


Fig. 4 Upper plenum pressure

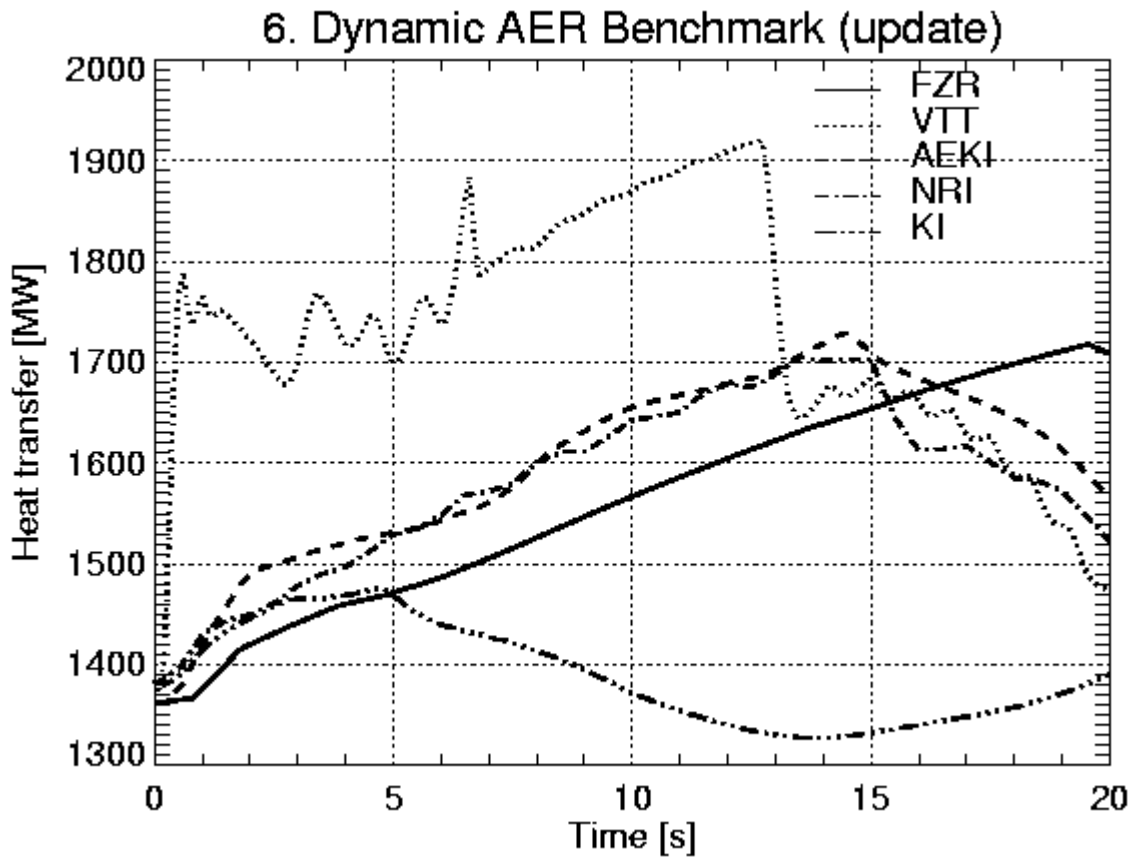


Fig. 5 Summary heat transfer in all steam generators

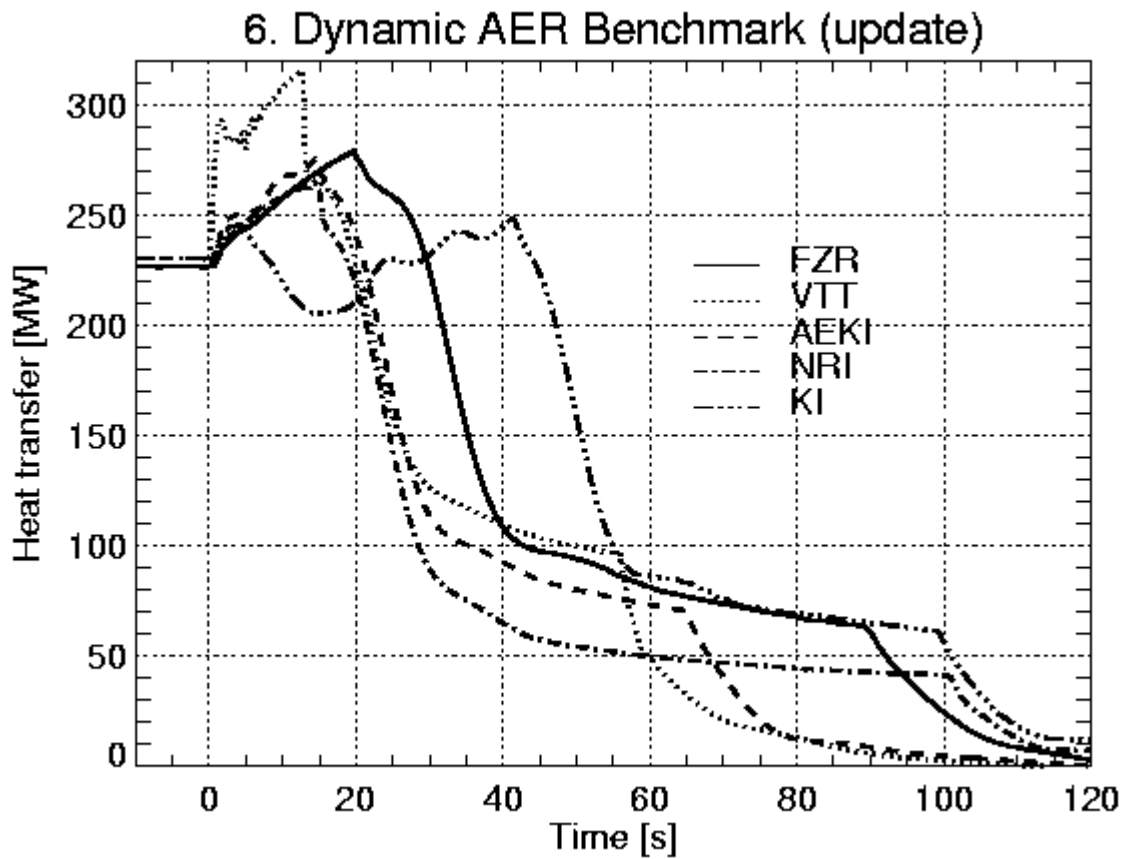


Fig. 6 Heat transfer averaged over all intact steam generators

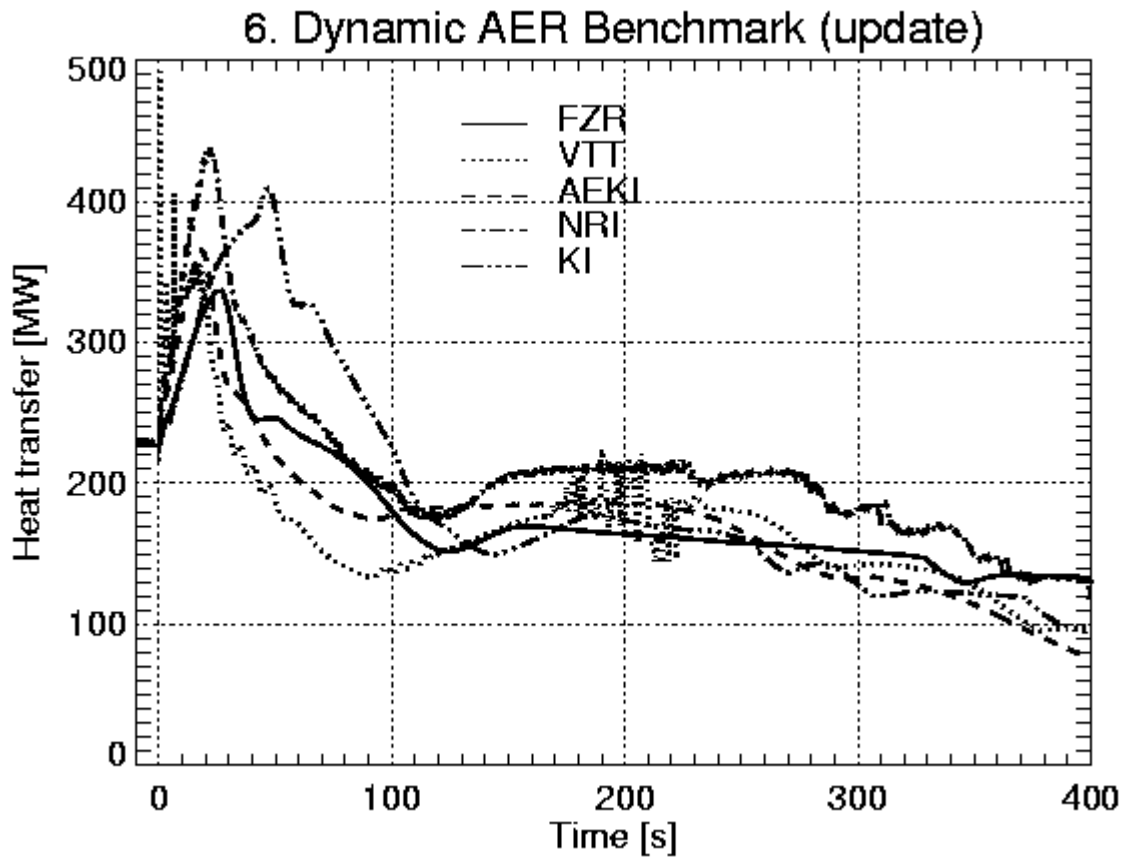


Fig. 7 Heat transfer in steam generator 1

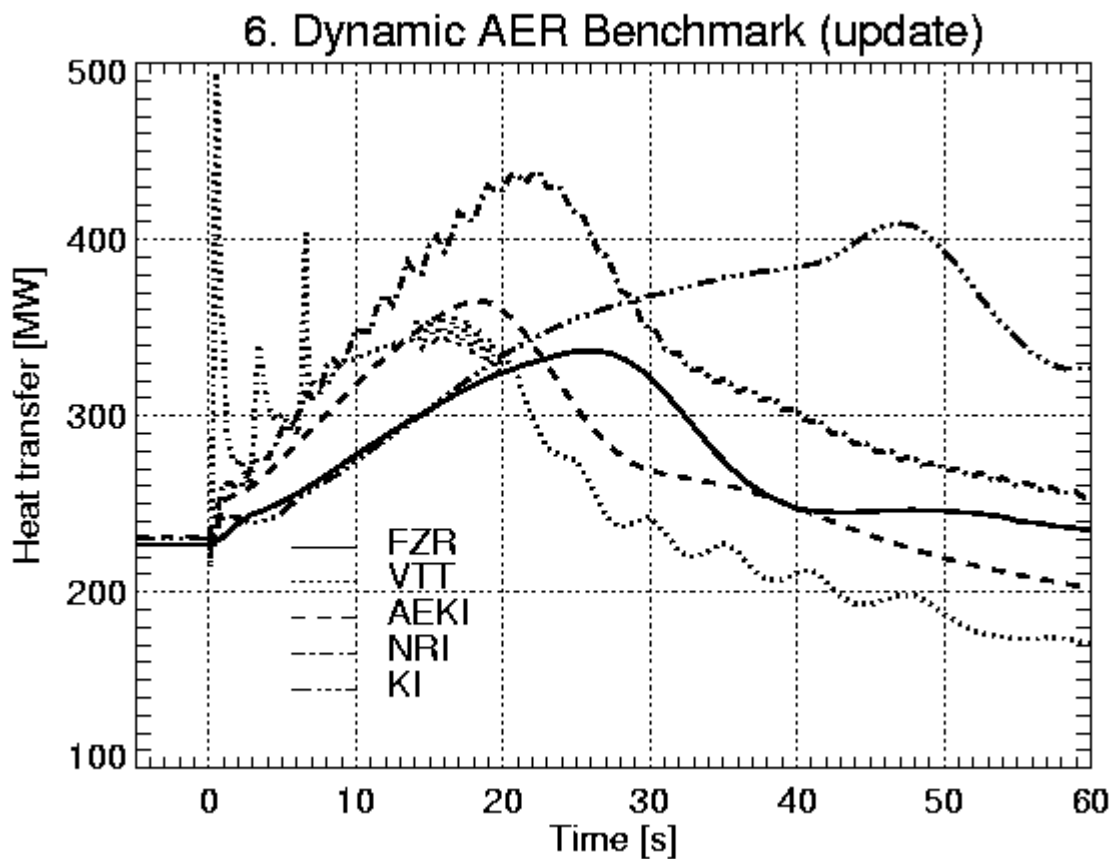


Fig. 8 Heat transfer in steam generator 1 (zoom)

### 6. Dynamic AER Benchmark (update)

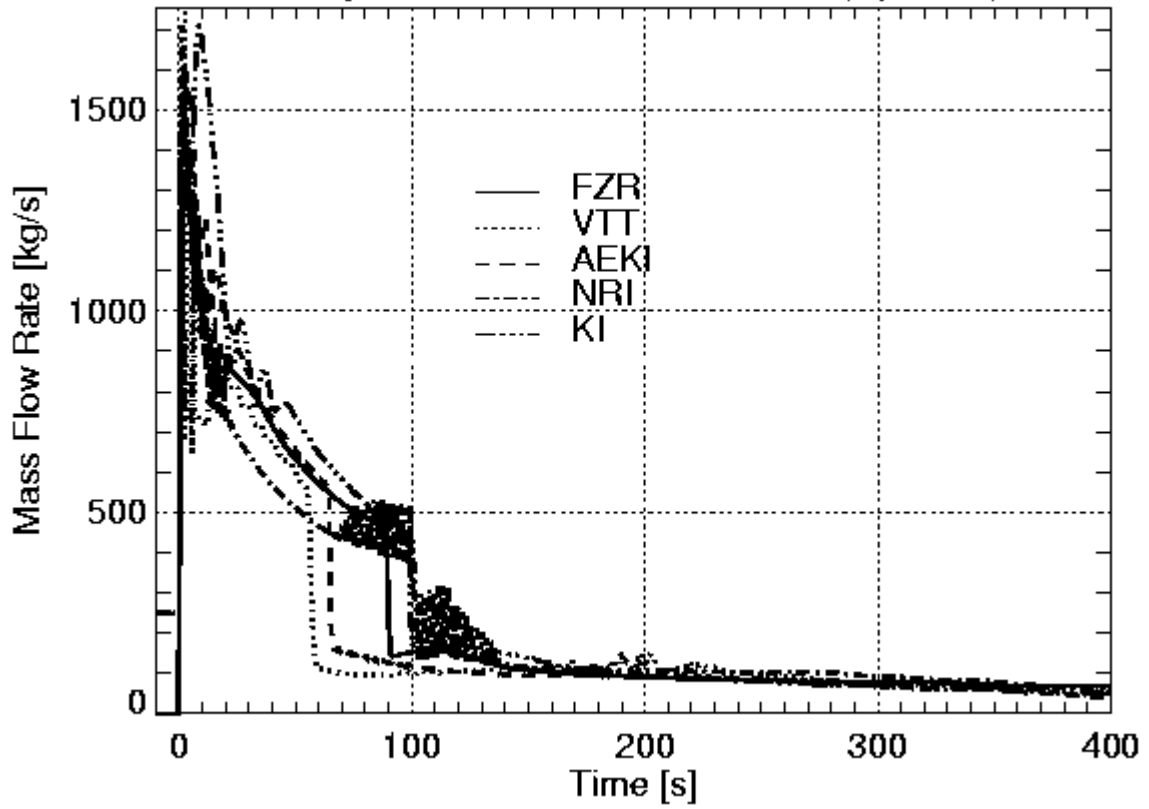


Fig. 9 Leak mass flow rate

### 6. Dynamic AER Benchmark (update)

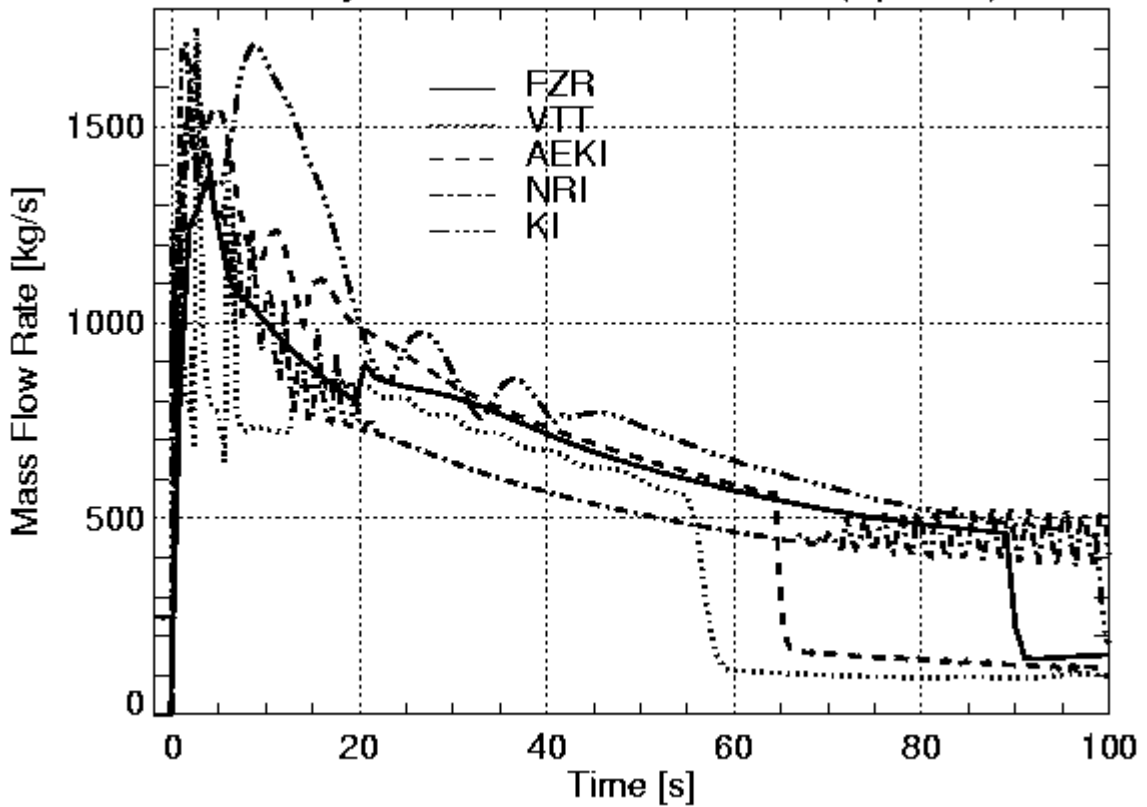


Fig. 10 Leak mass flow rate (zoom)

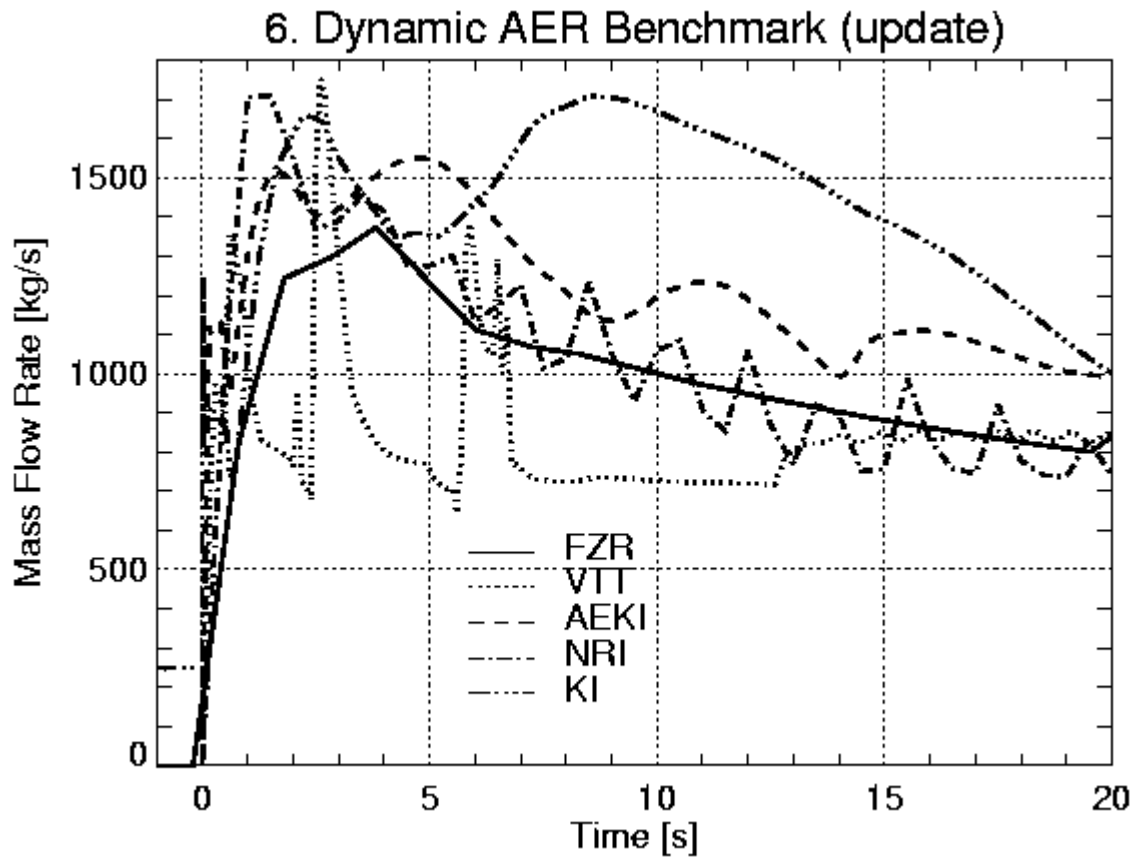


Fig. 11 Leak mass flow rate (zoom)

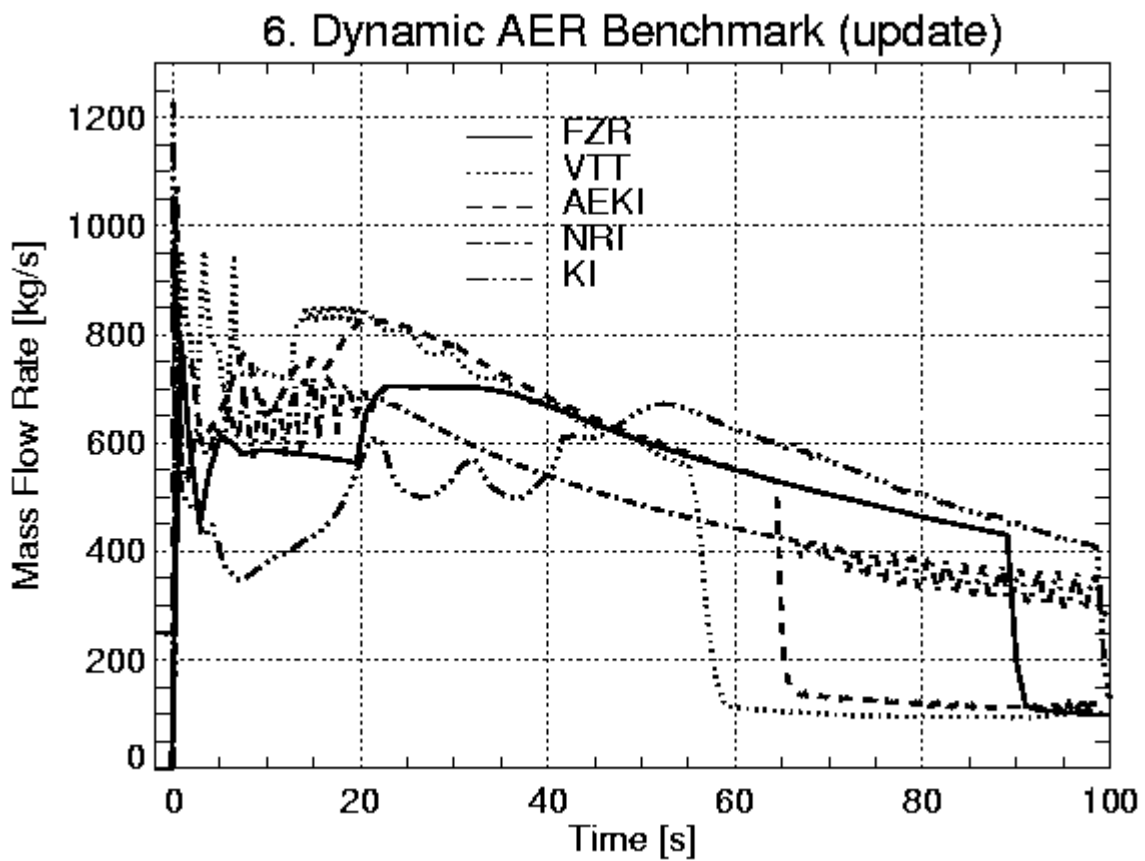


Fig. 12 Leak steam mass flow rate

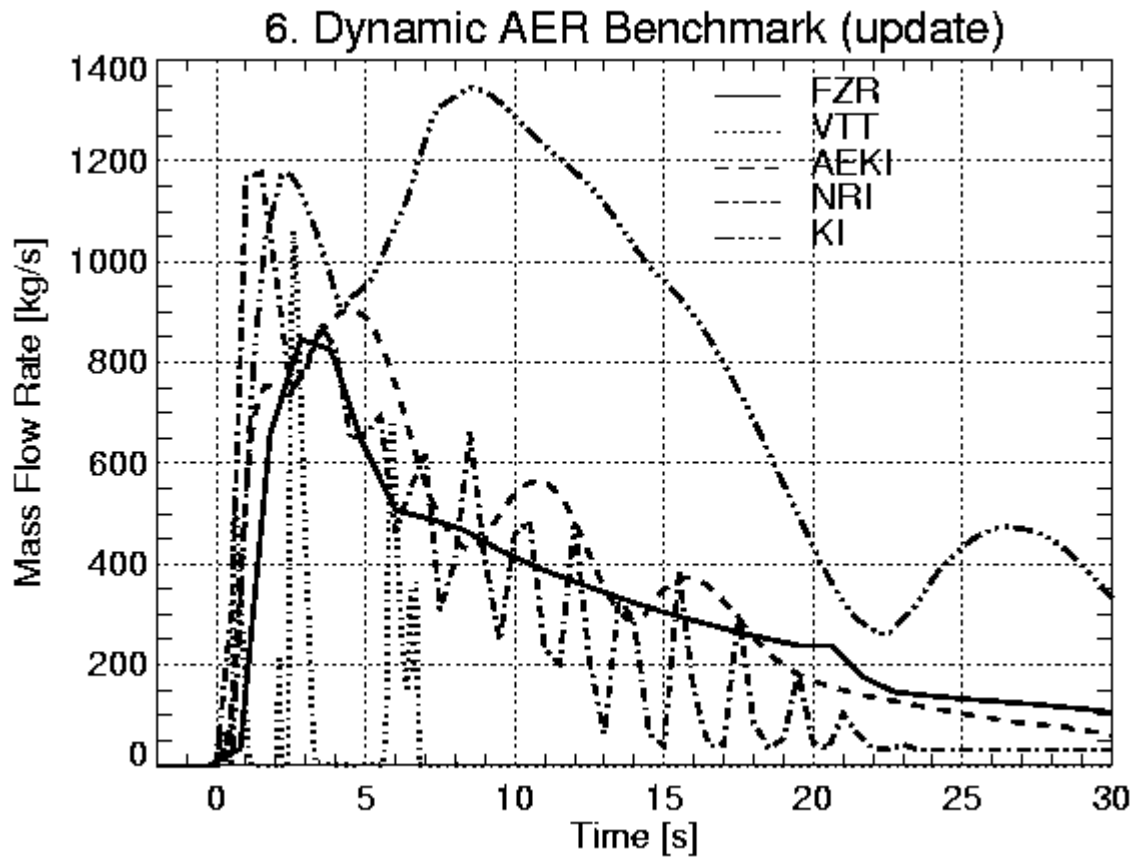


Fig. 13 Leak liquid mass flow rate

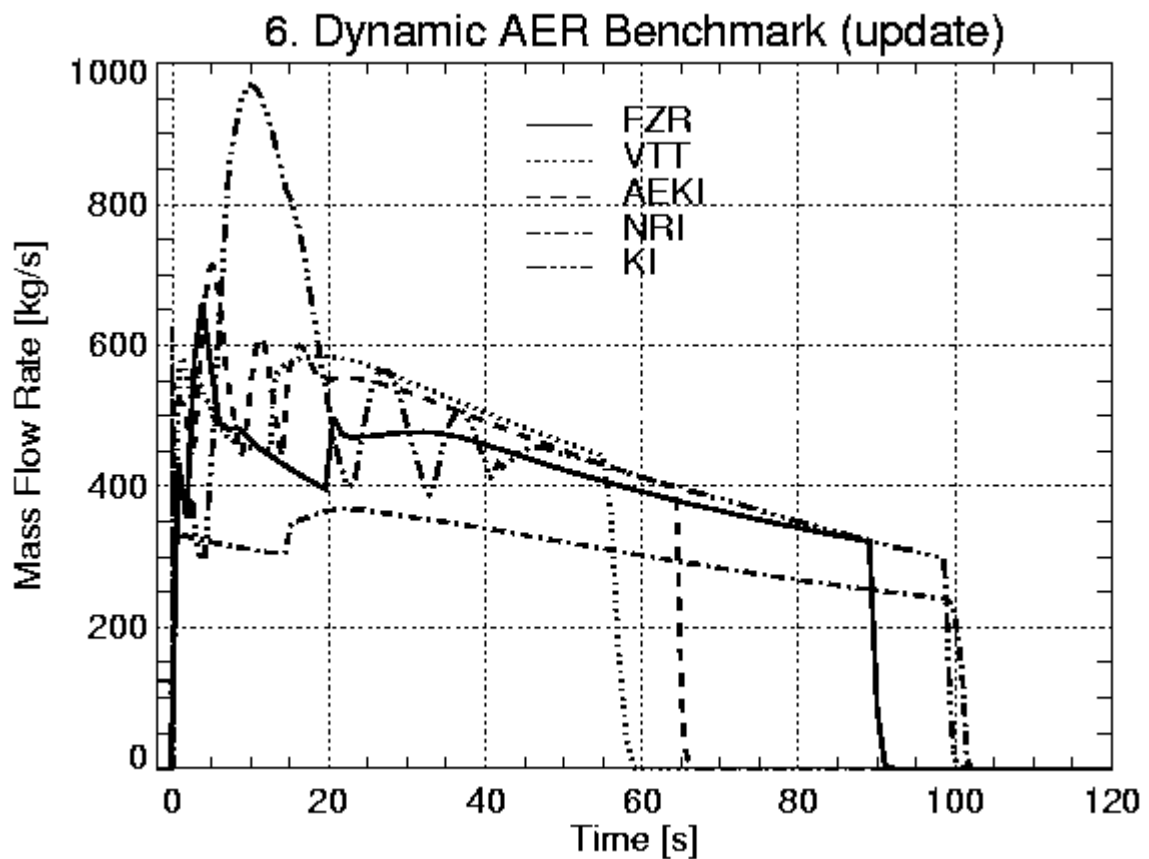


Fig. 14 Leak mass flow rate from main steam header side

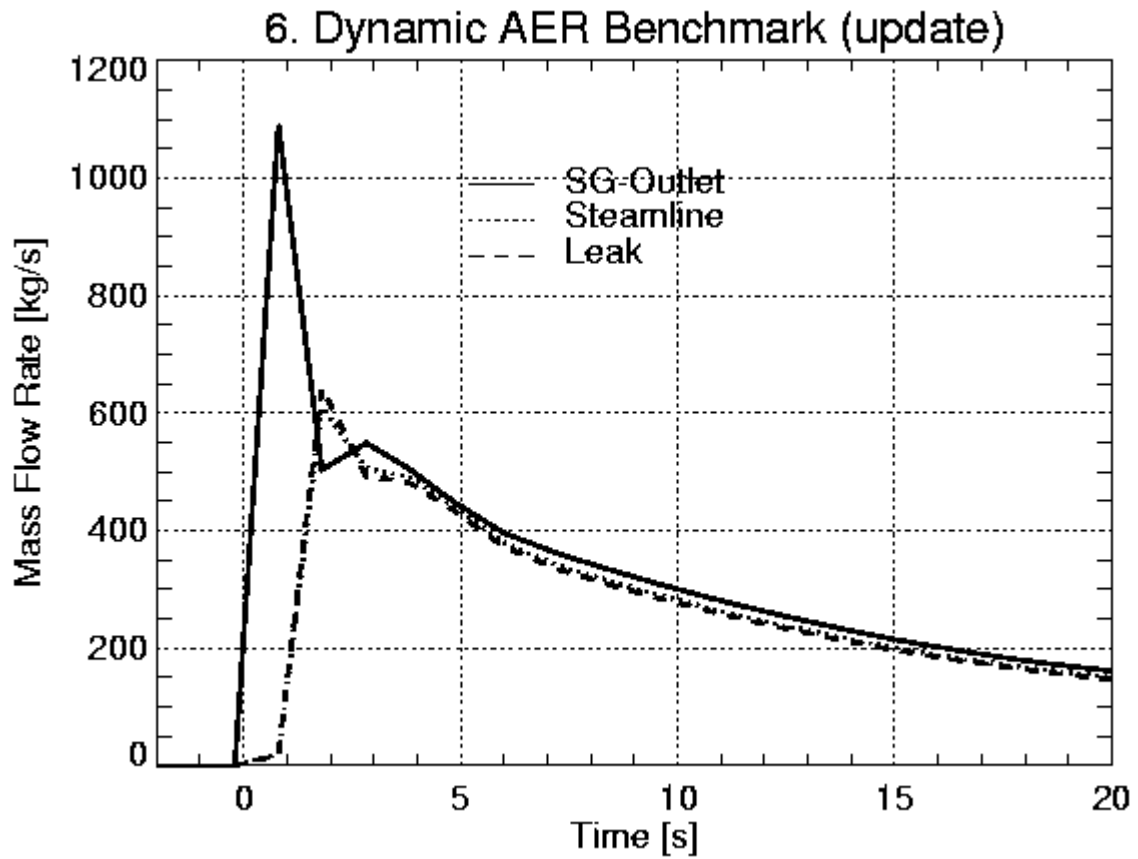


Fig. 15 Liquid mass flow rate at different points at the flow path (FZR)

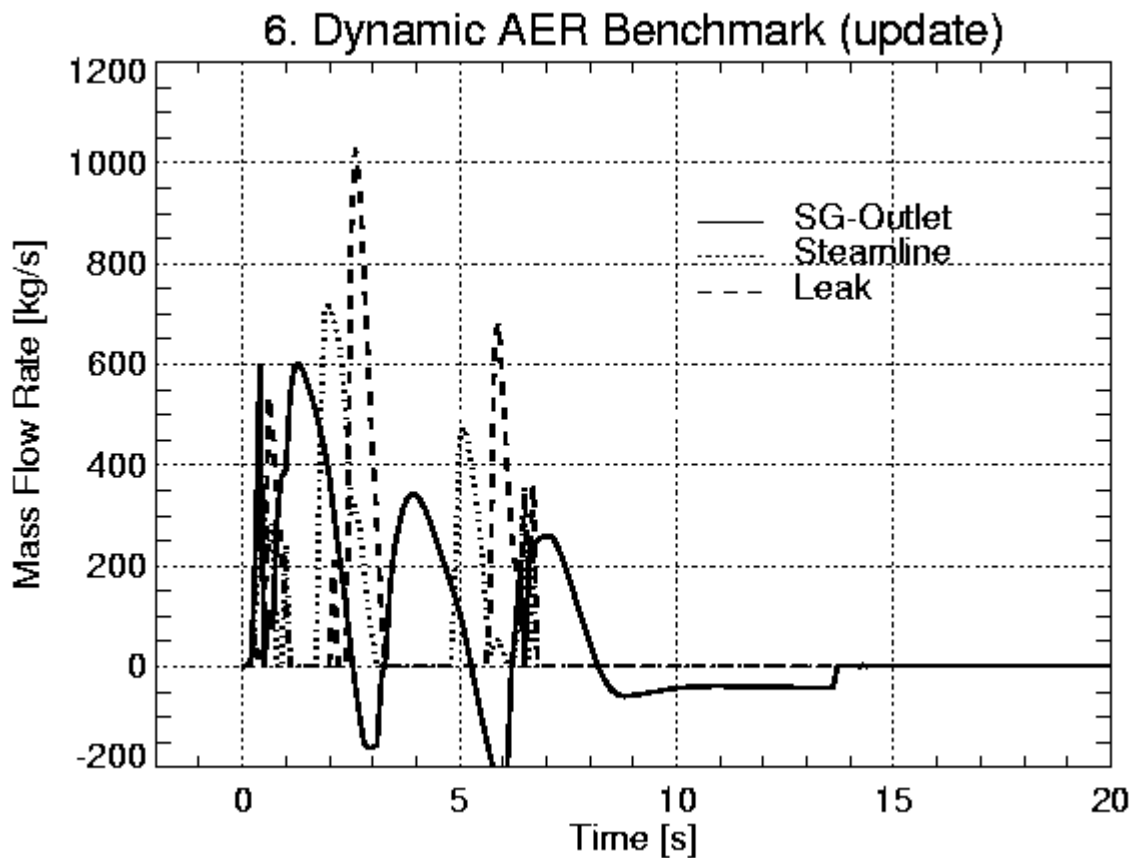


Fig. 16 Liquid mass flow rate at different points at the flow path (VTT)

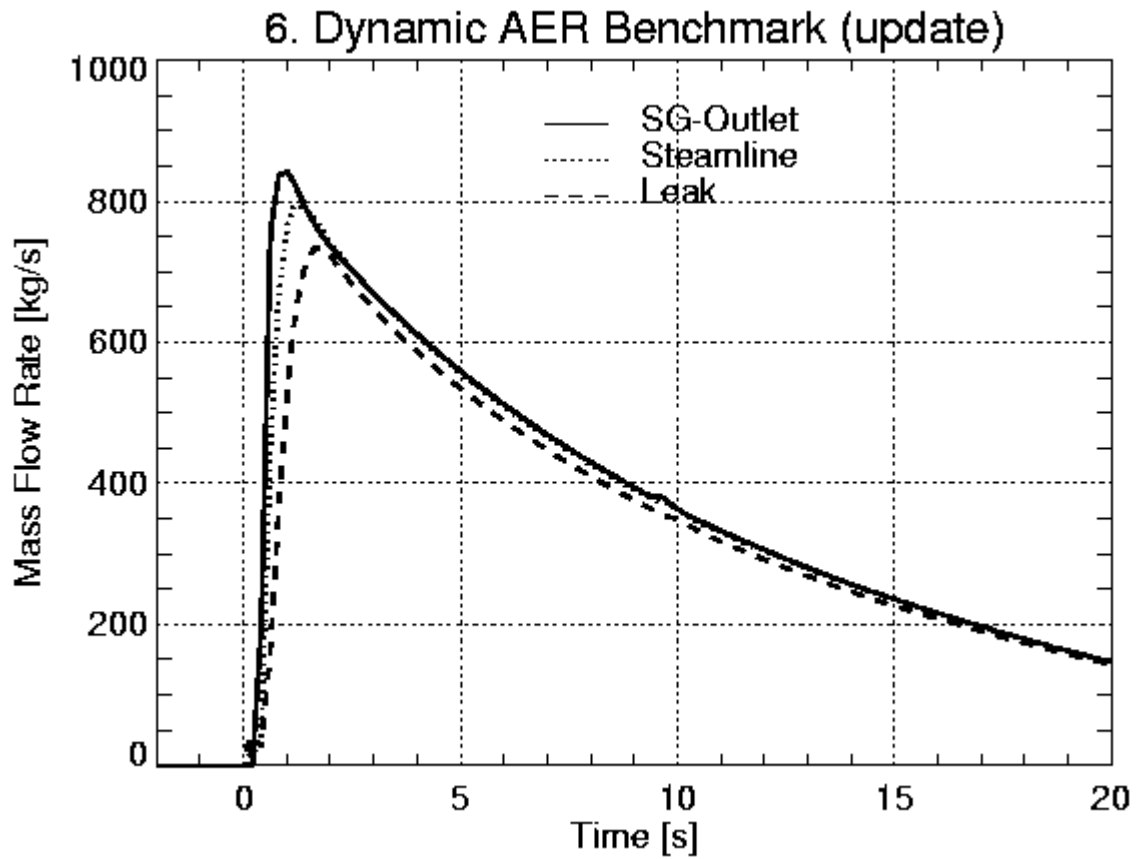


Fig. 17 Liquid mass flow rate at different points at the flow path (AEKI)

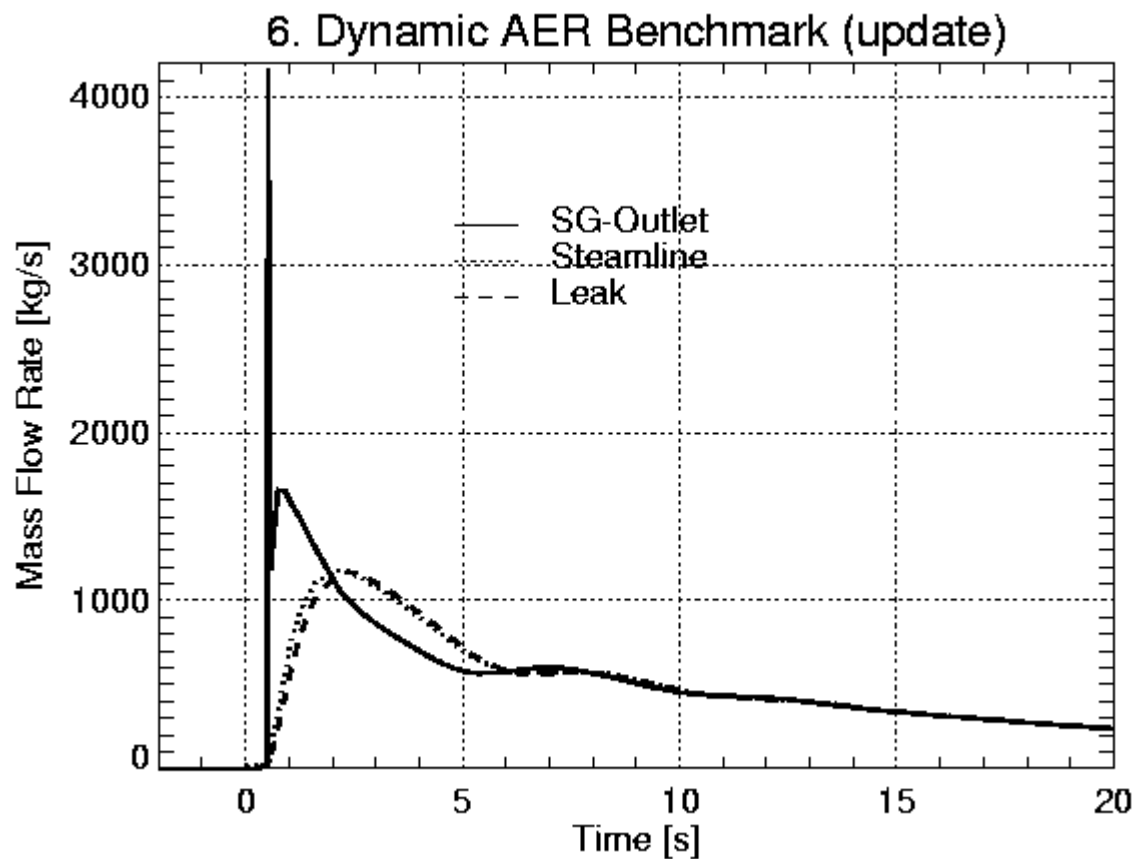


Fig. 18 Liquid mass flow rate at different points at the flow path (KI)

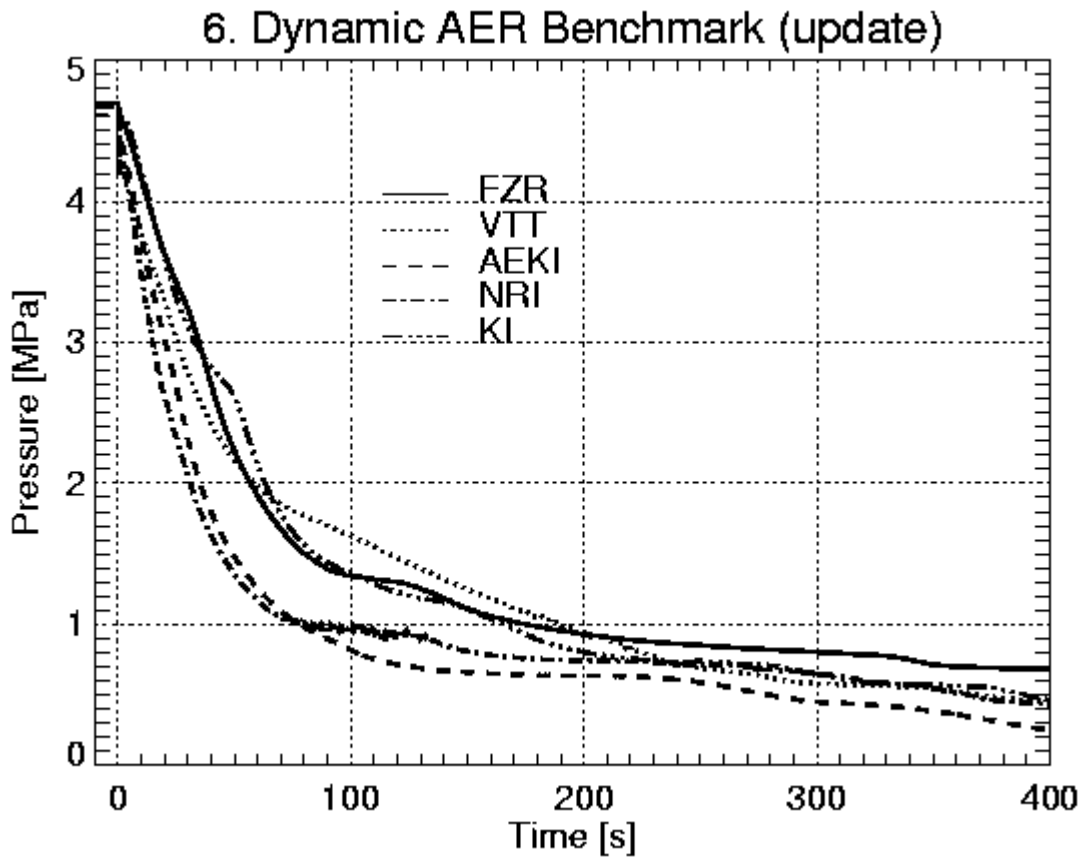


Fig. 19 Pressure in steam generator 1 (broken line)

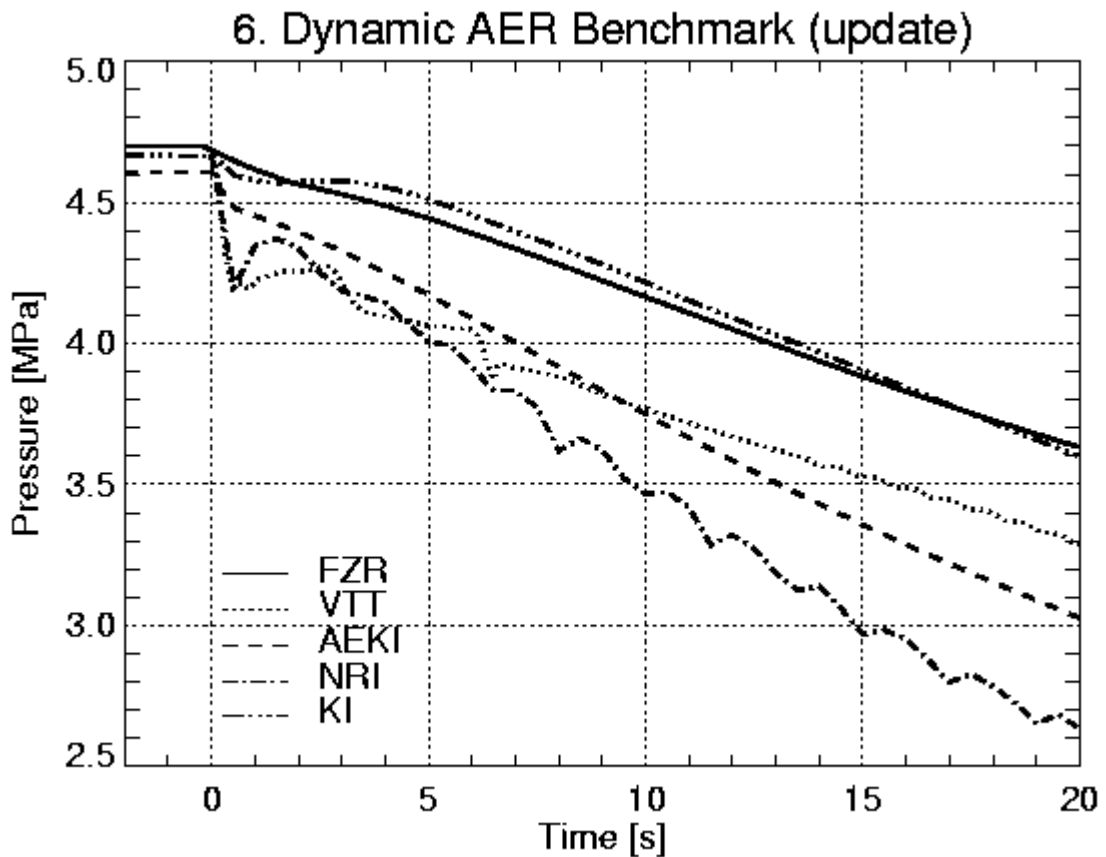


Fig. 20 Pressure in steam generator 1 (zoom)

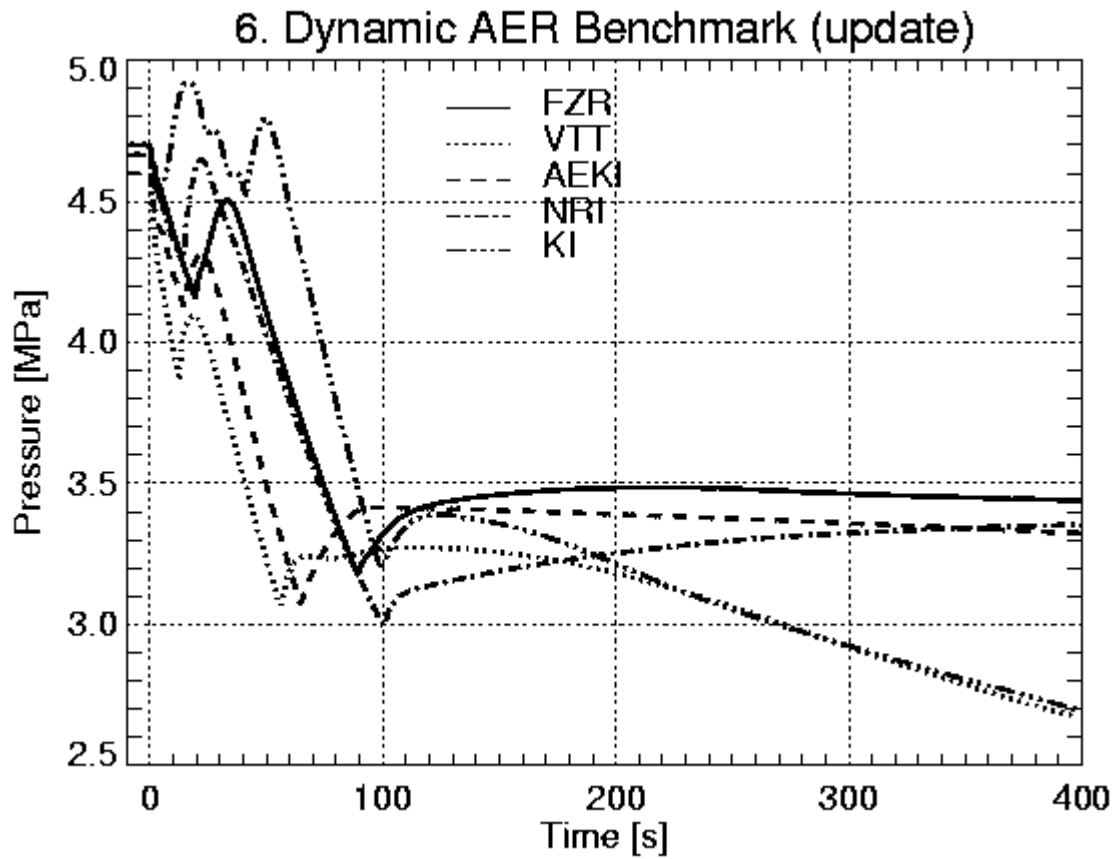


Fig. 21 Pressure averaged over all intact steam generators

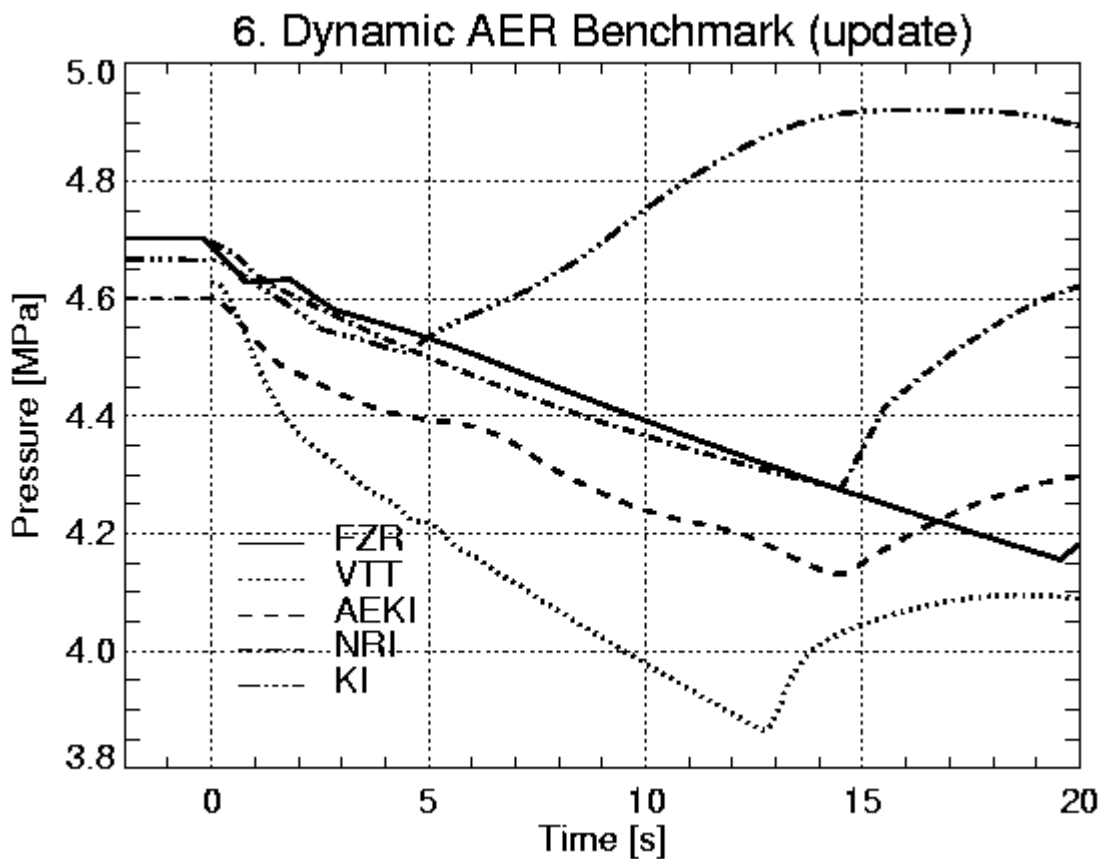


Fig. 22 Pressure averaged over all intact steam generators (zoom)

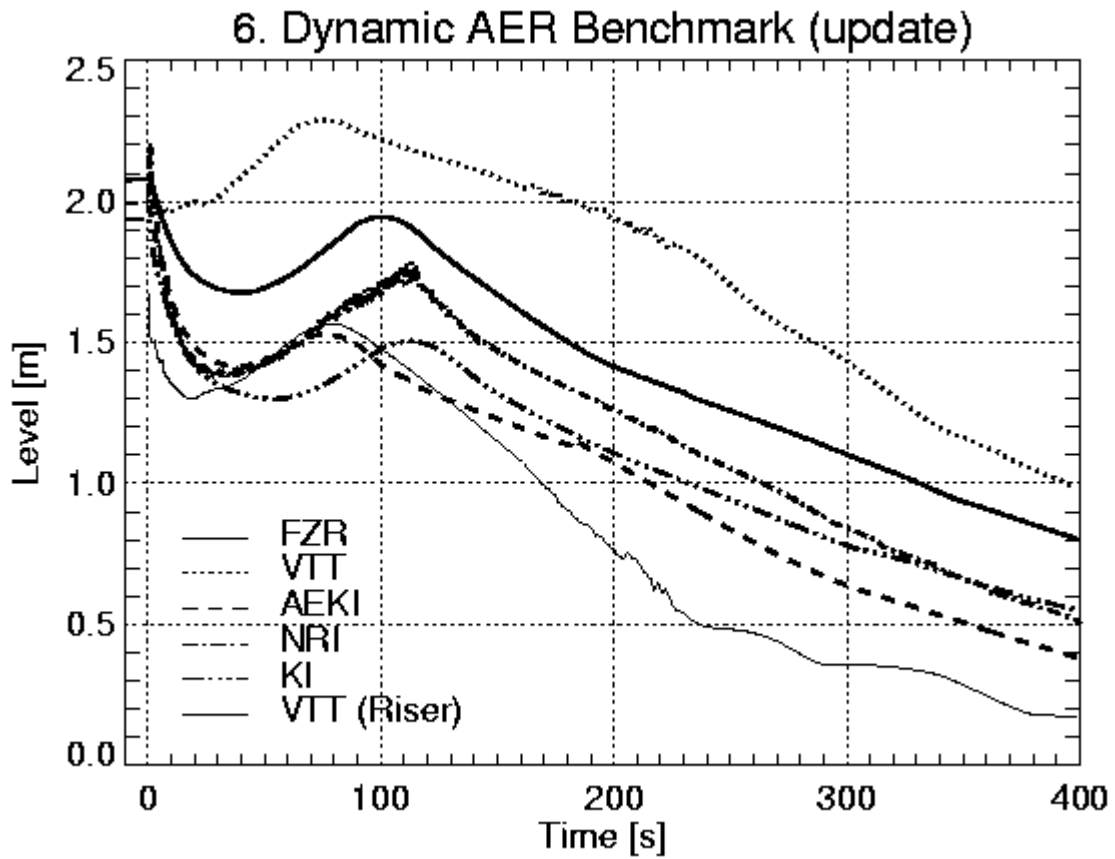


Fig. 23 Collapsed level in steam generator 1 (broken line)

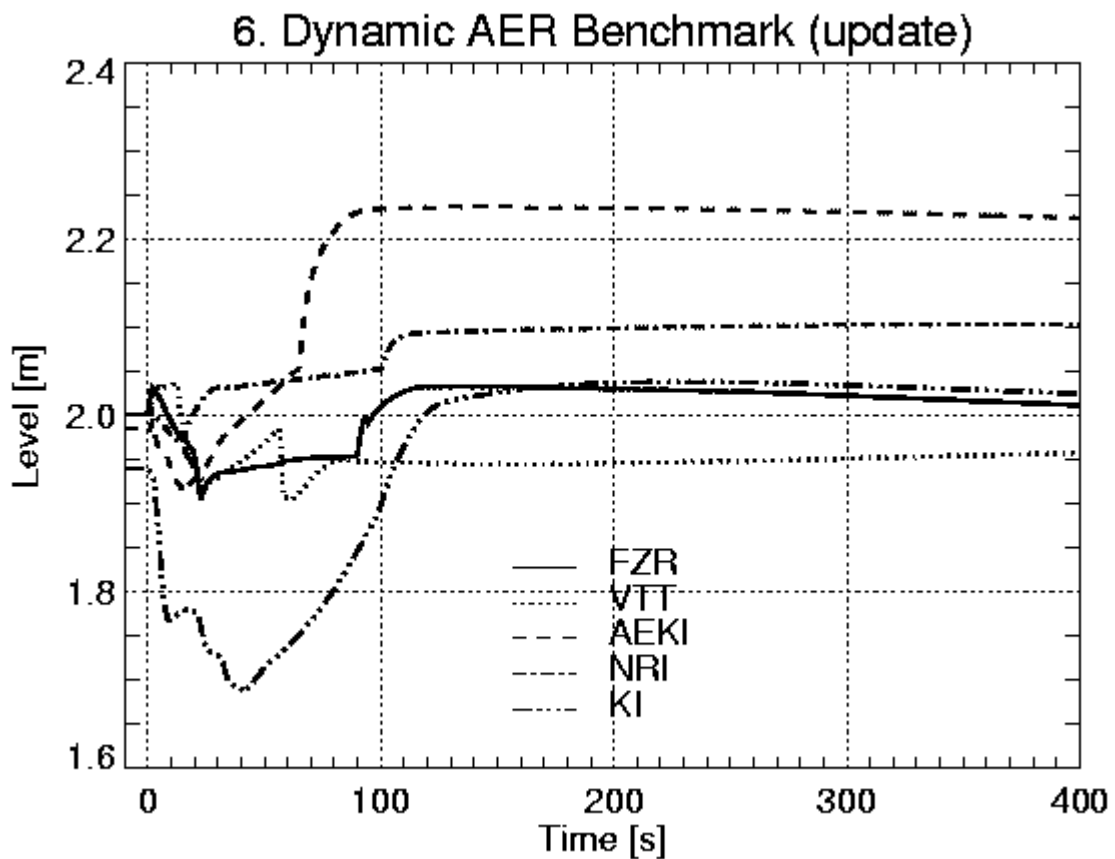


Fig. 24 Collapsed level averaged over all intact steam generators

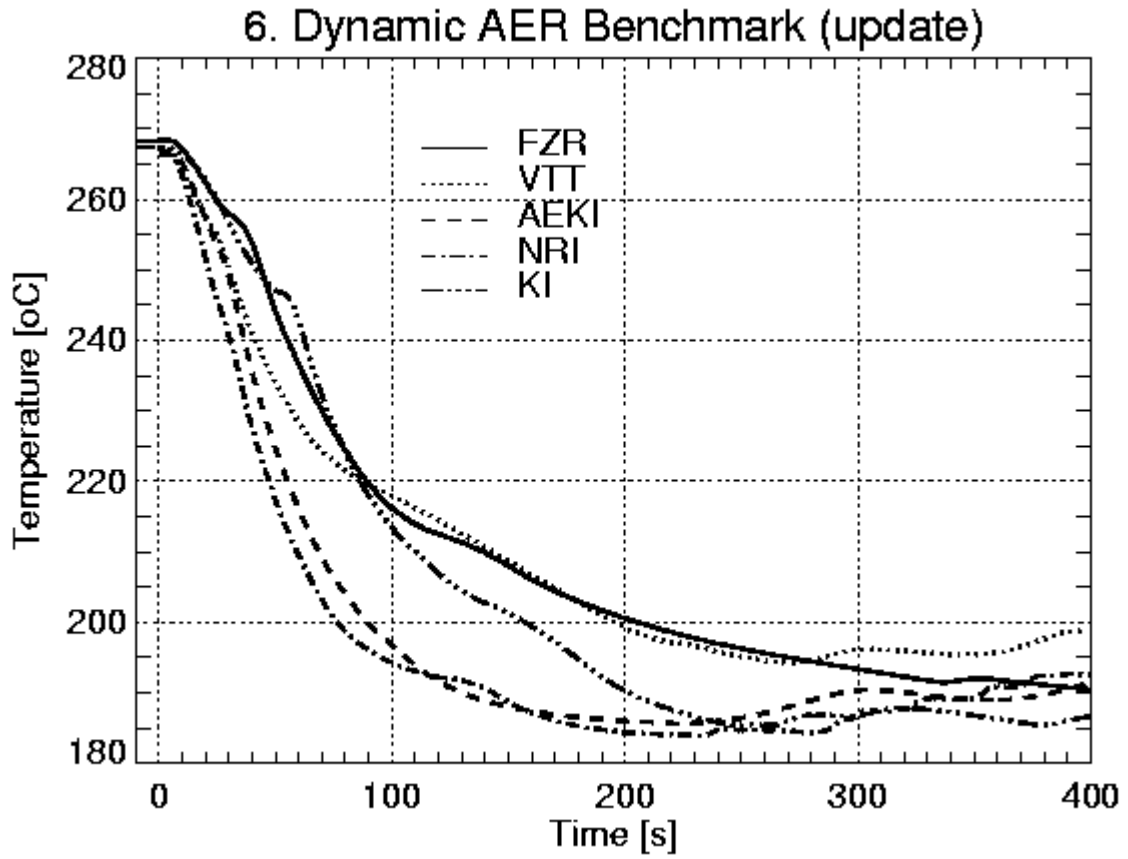


Fig. 25 Coolant temperature at core inlet (sector 1)

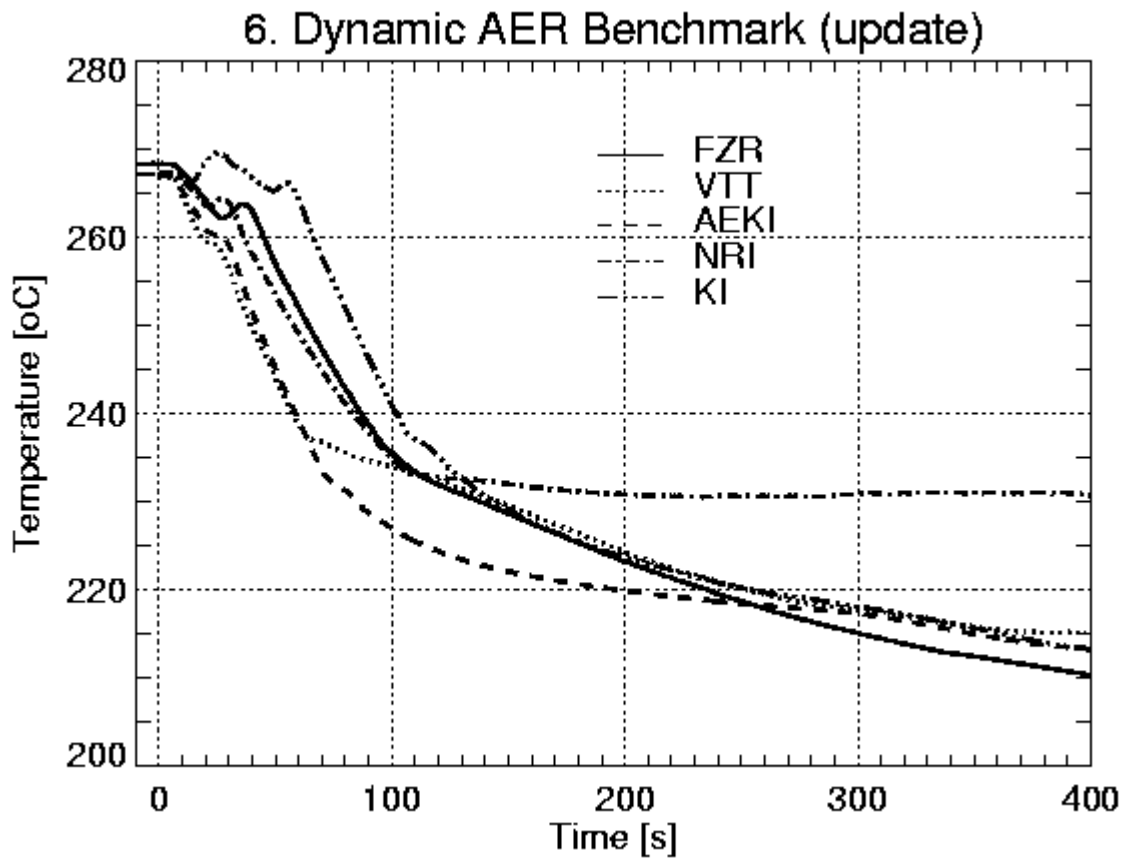


Fig. 26 Coolant temperature at core inlet (sector 2)

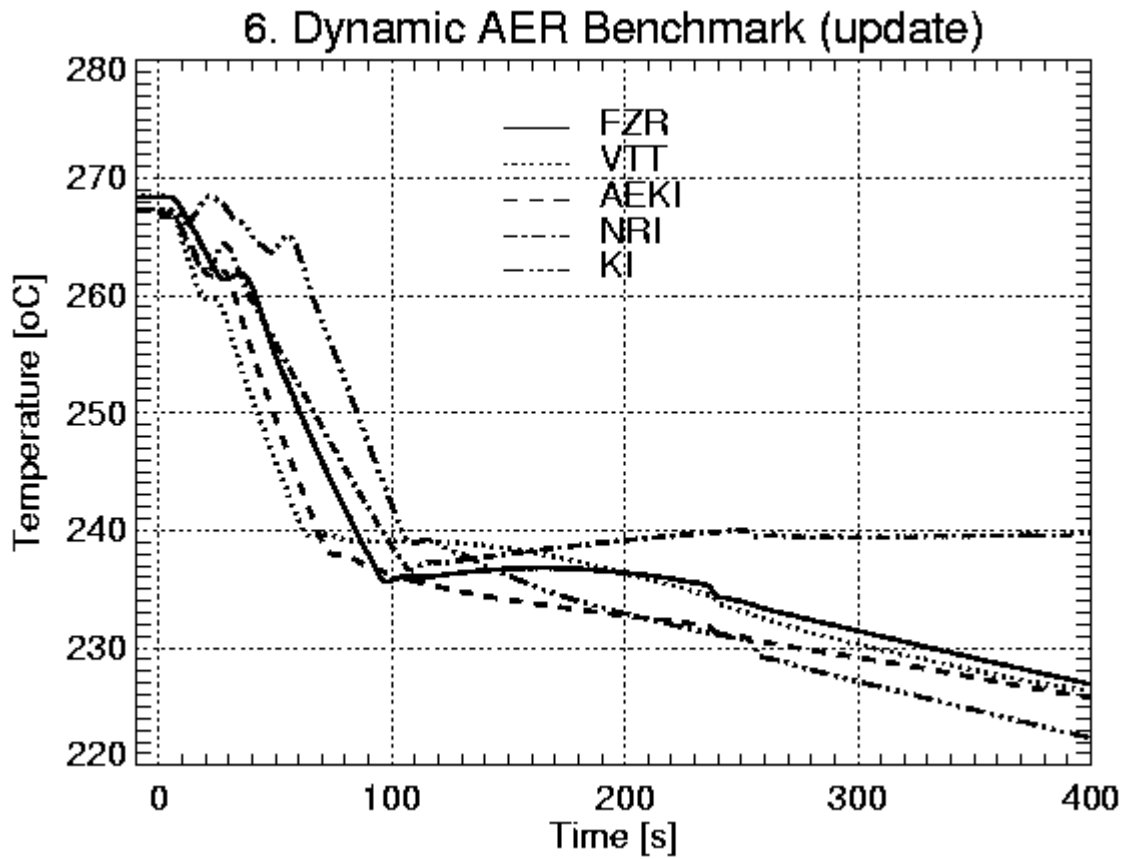


Fig. 27 Coolant temperature at core inlet (sector 3)

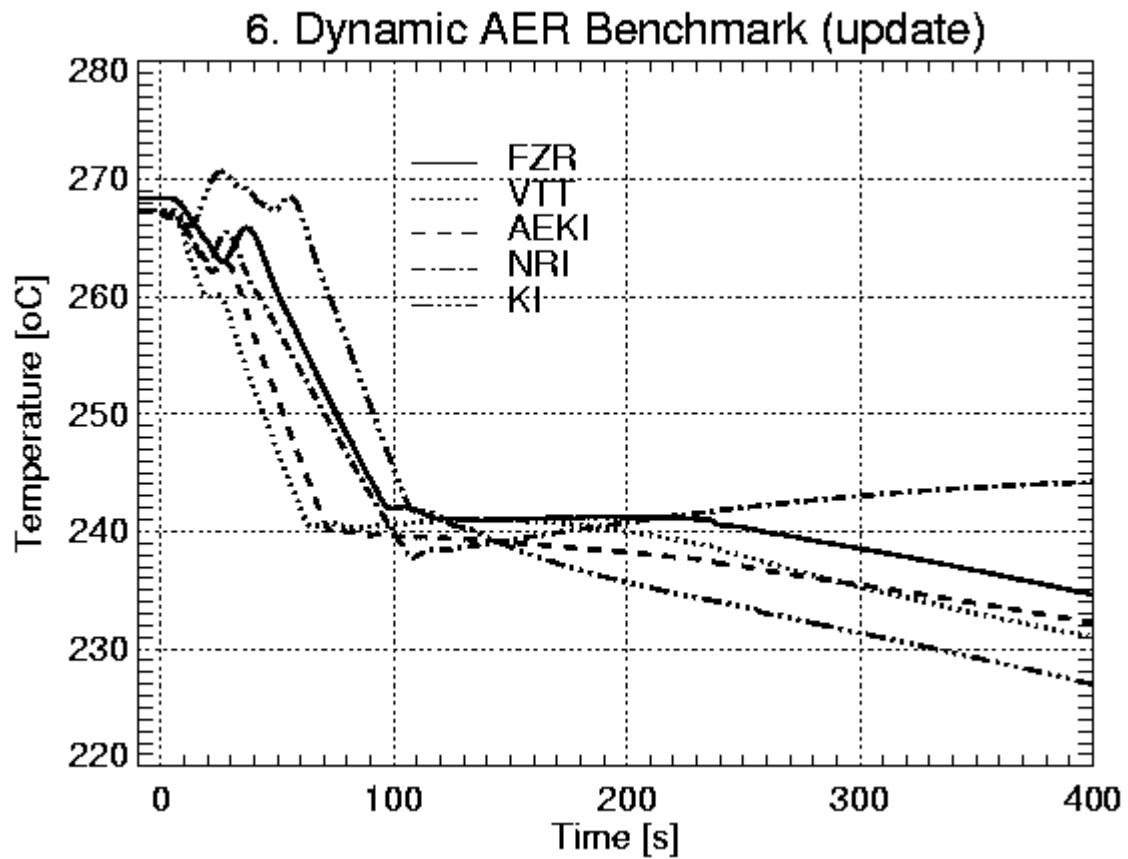


Fig. 28 Coolant temperature at core inlet (sector 4)

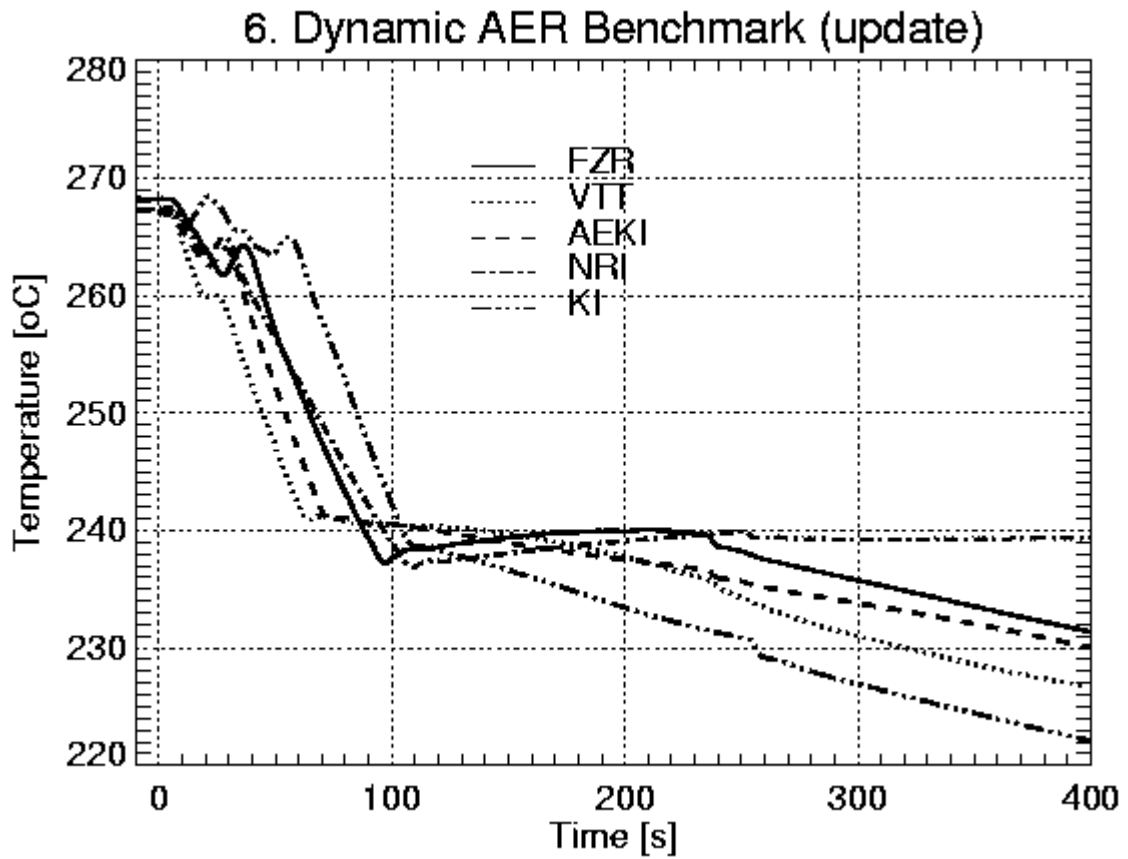


Fig. 29 Coolant temperature at core inlet (sector 5)

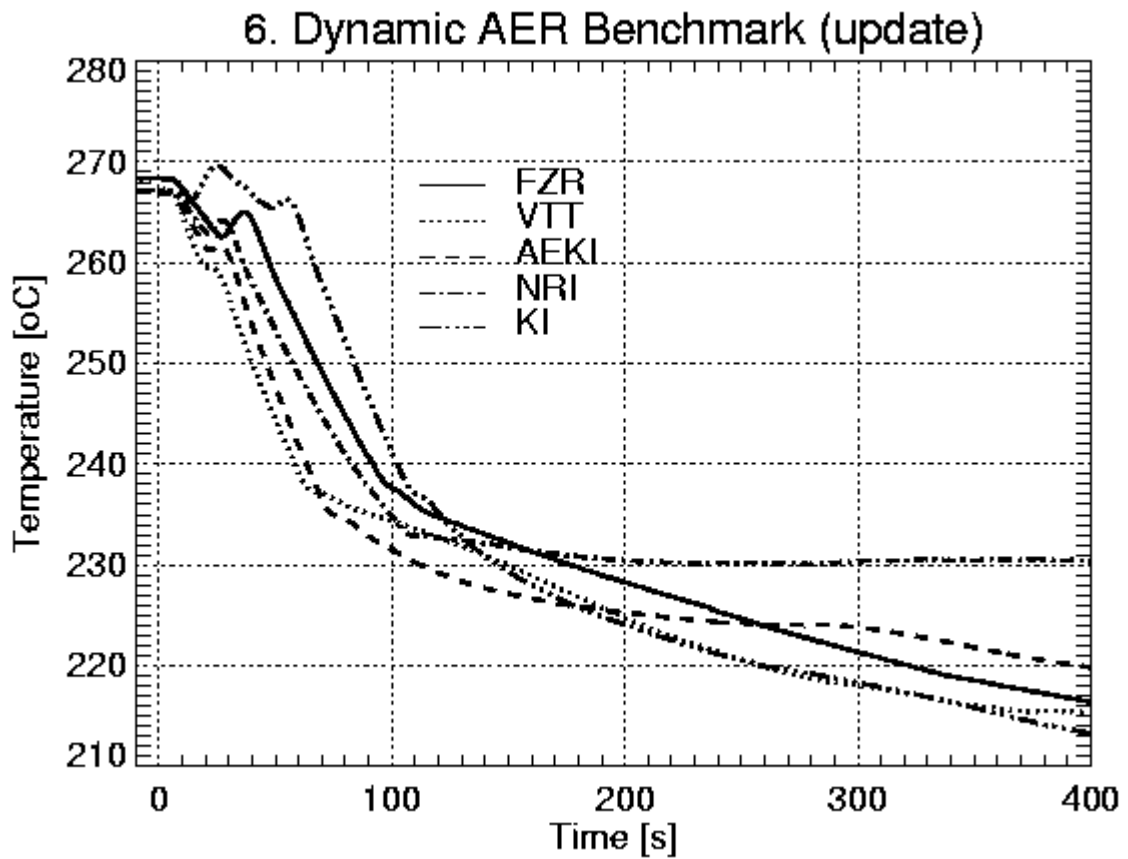


Fig. 30 Coolant temperature at core inlet (sector 6)

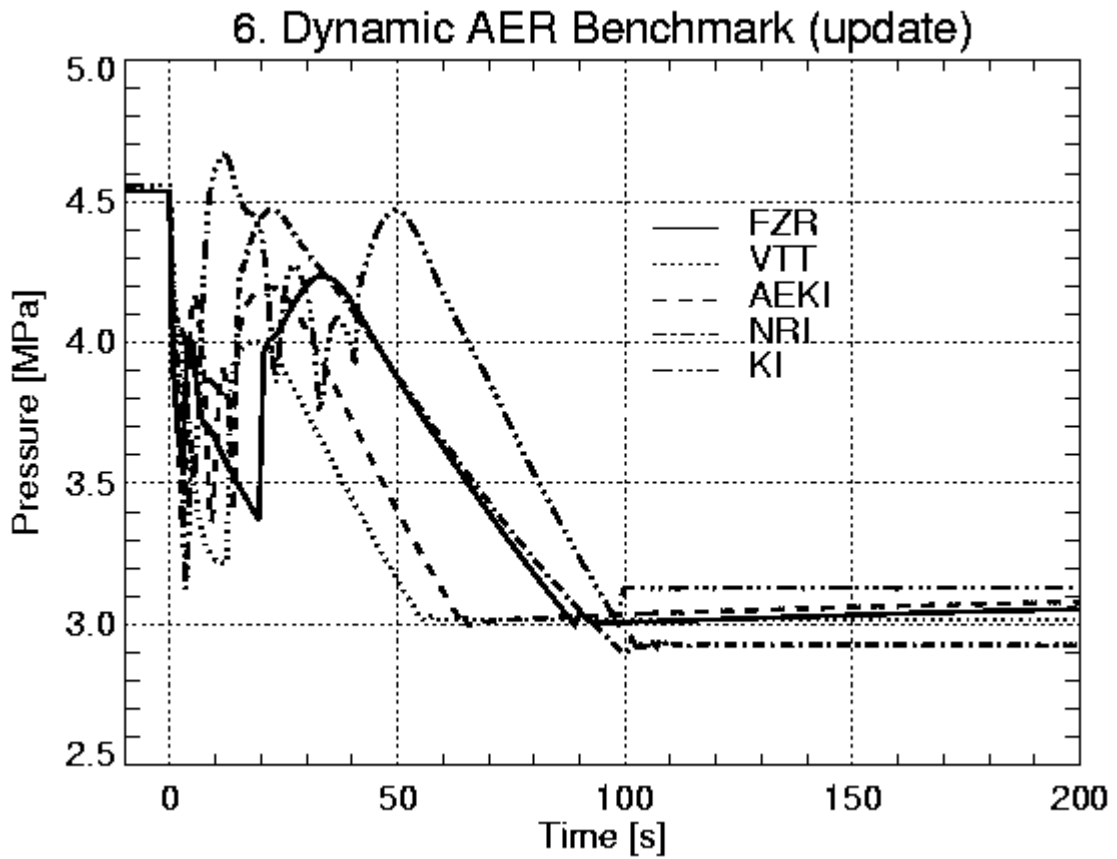


Fig. 31 Pressure in main steam header

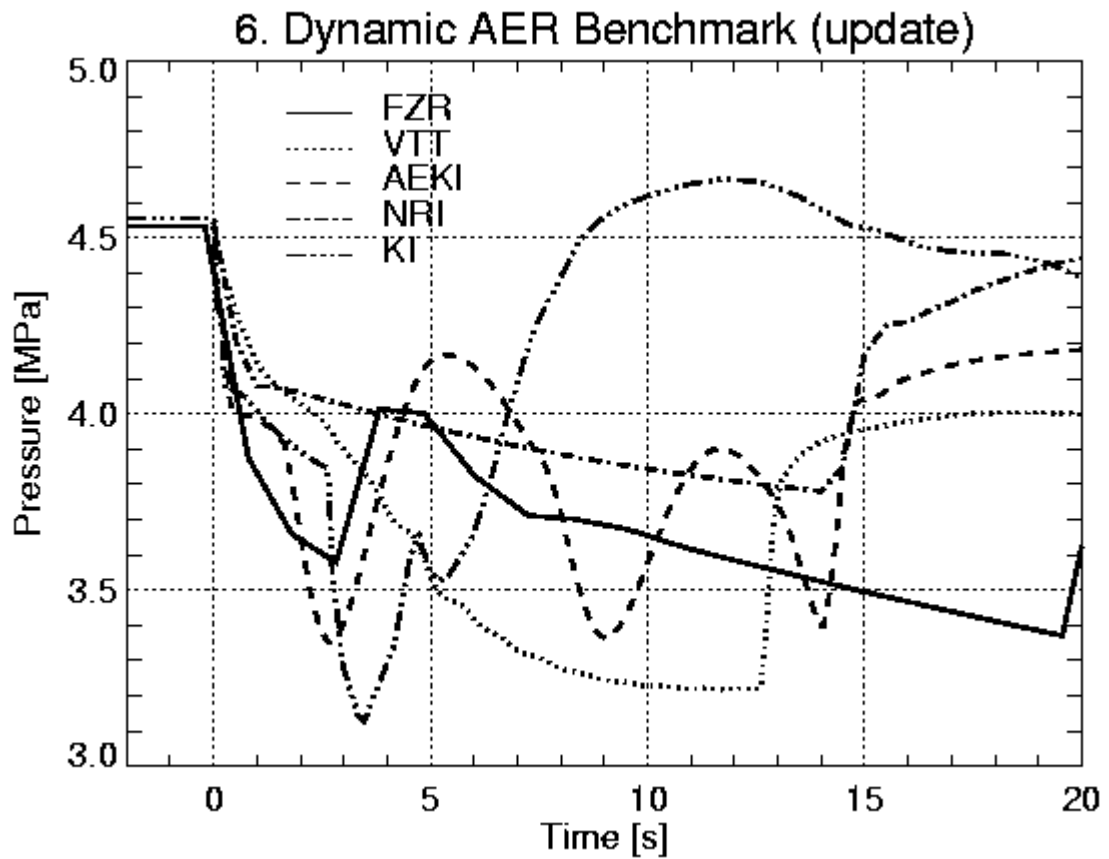


Fig. 32 Pressure in main steam header (zoom)

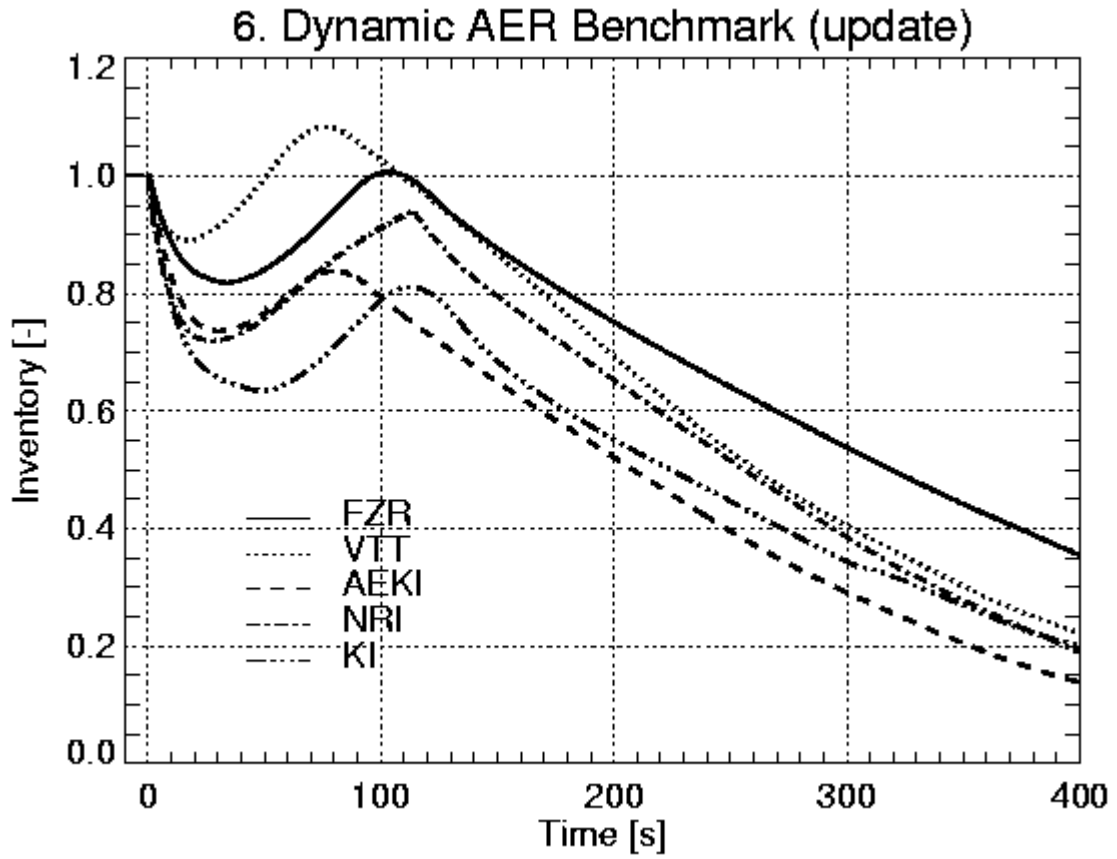


Fig. 33 Normalized broken steam generator inventory

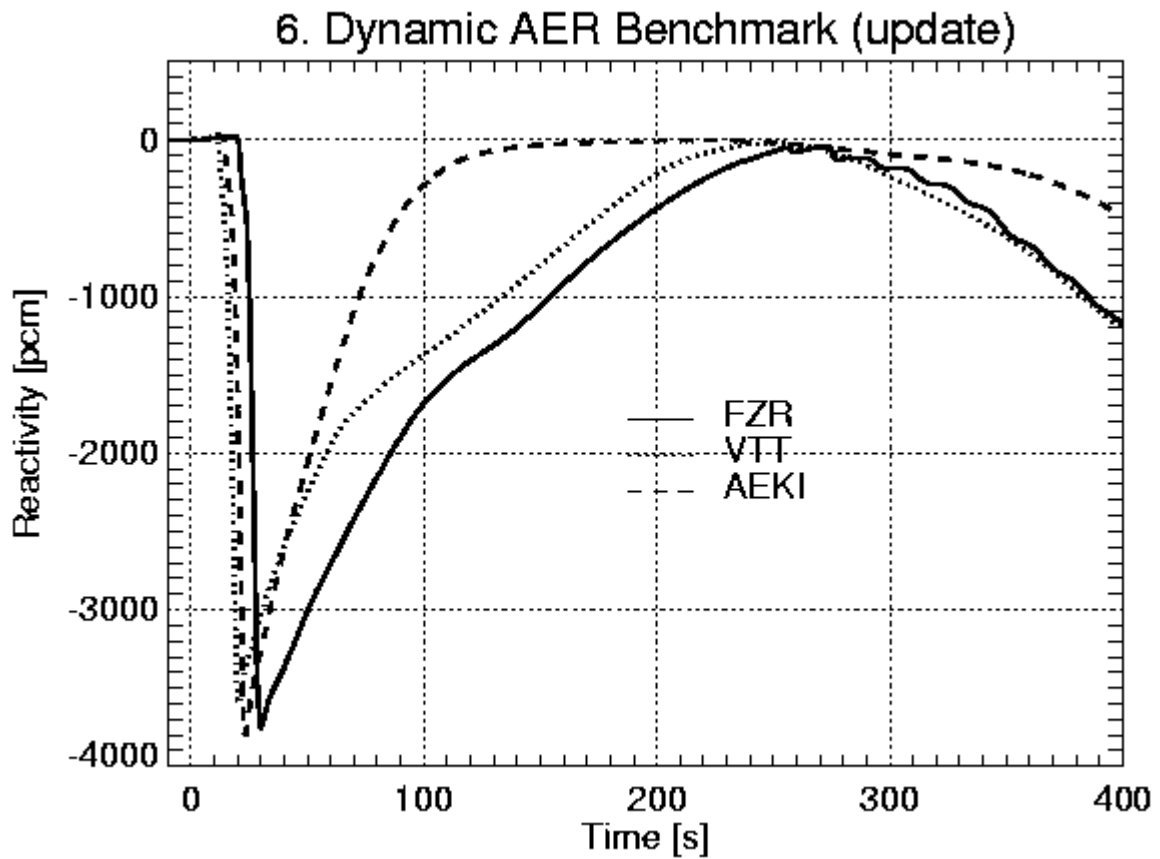


Fig. 34 Dynamic reactivity during the transient

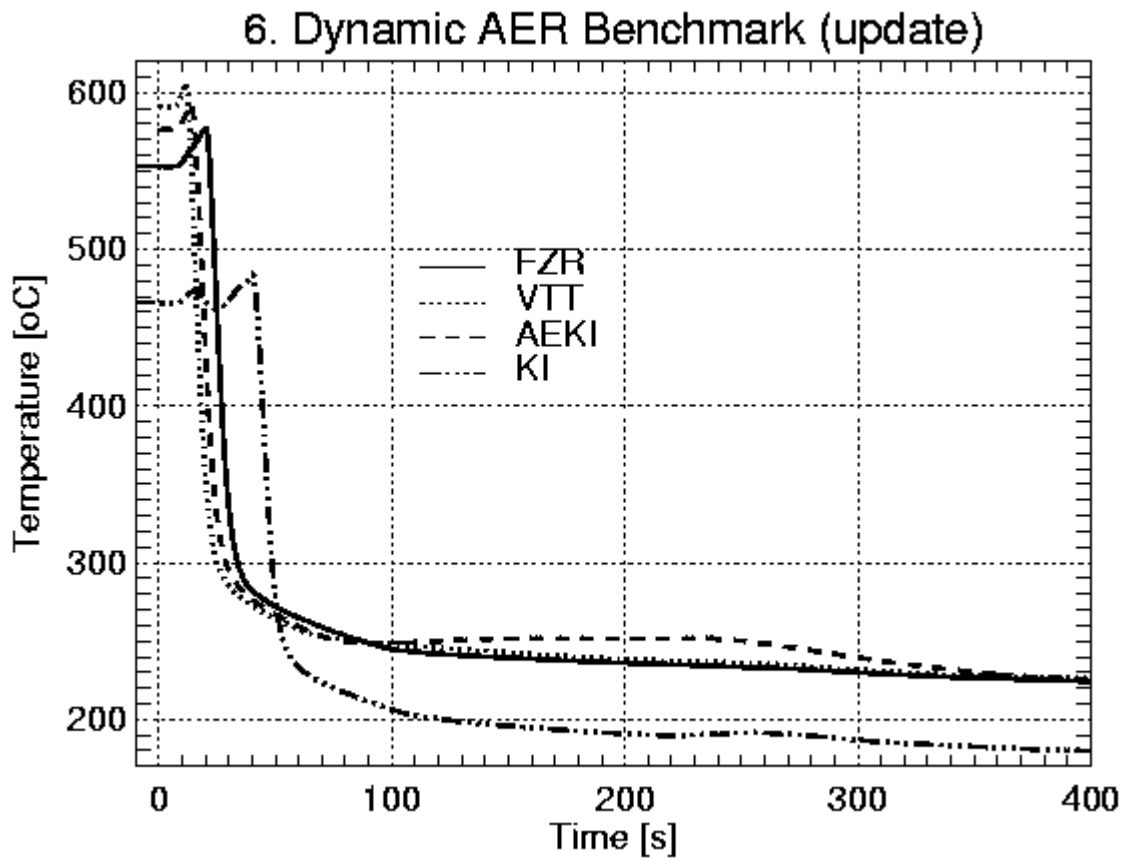


Fig. 35 Averaged fuel temperature

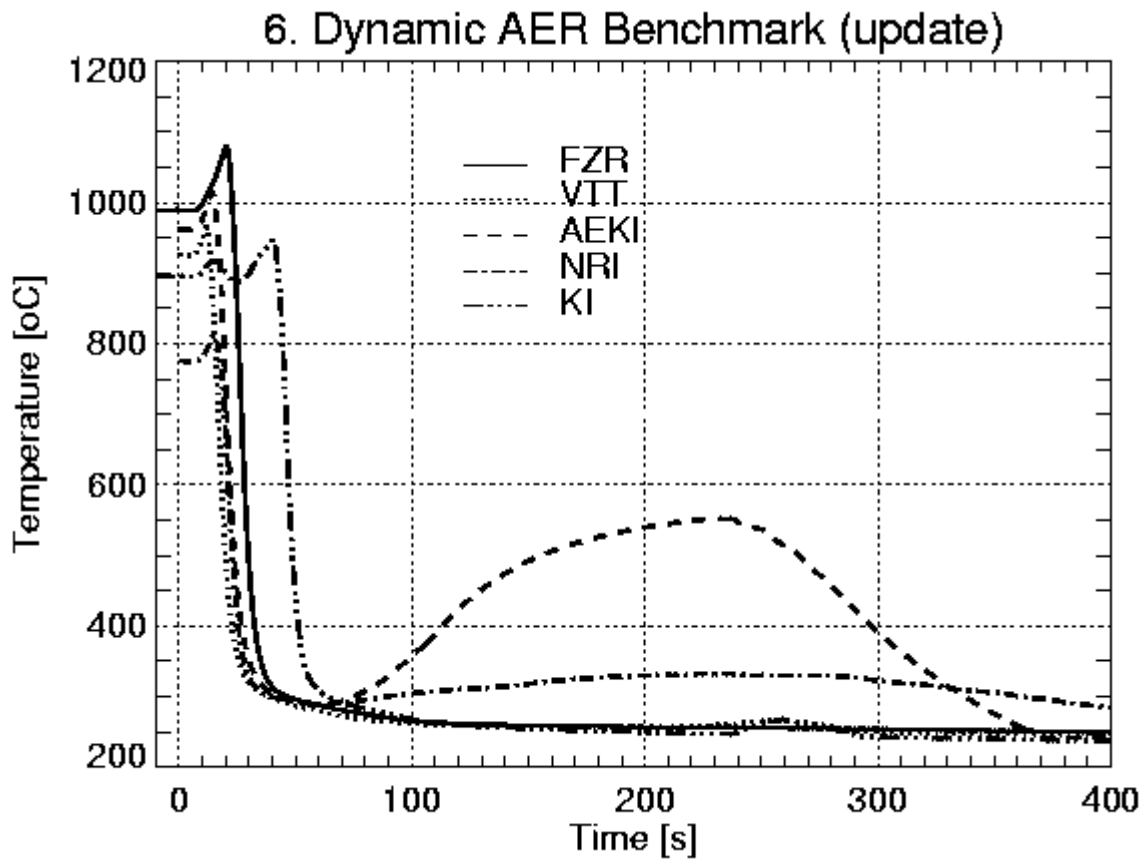


Fig. 36 Maximum fuel temperature

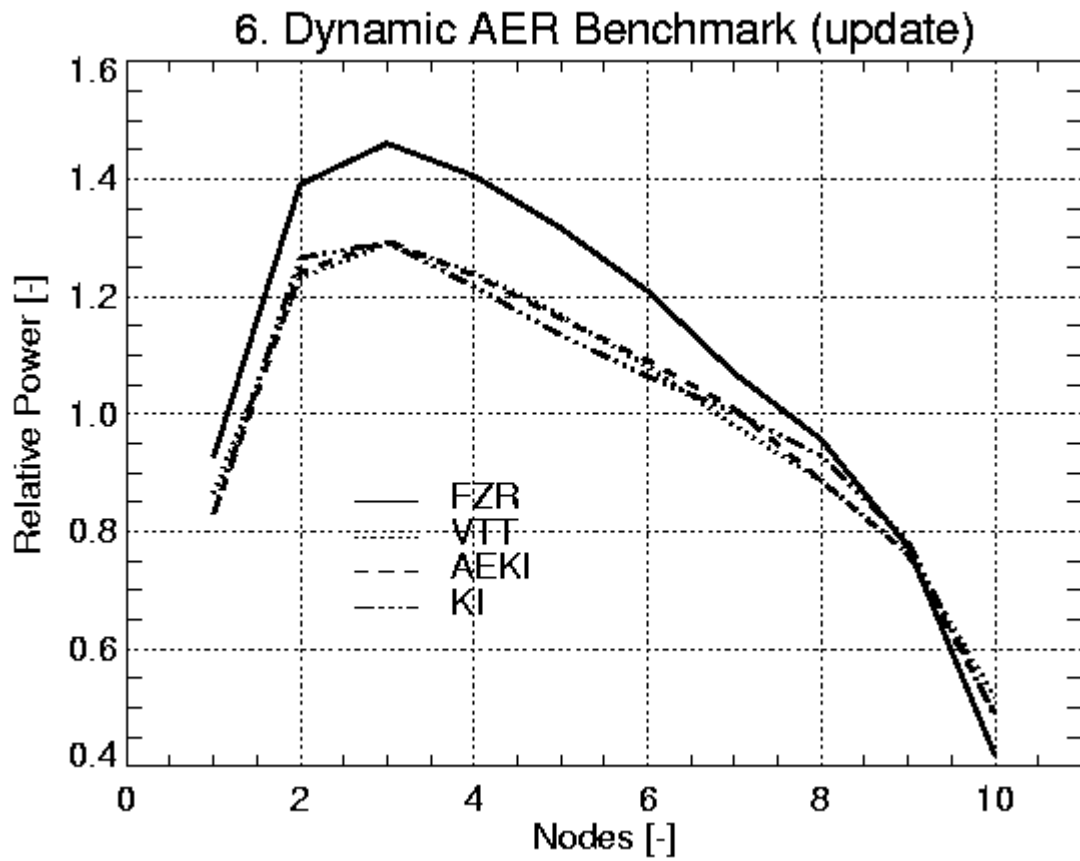


Fig. 37 Axial power distribution at the time of first power maximum

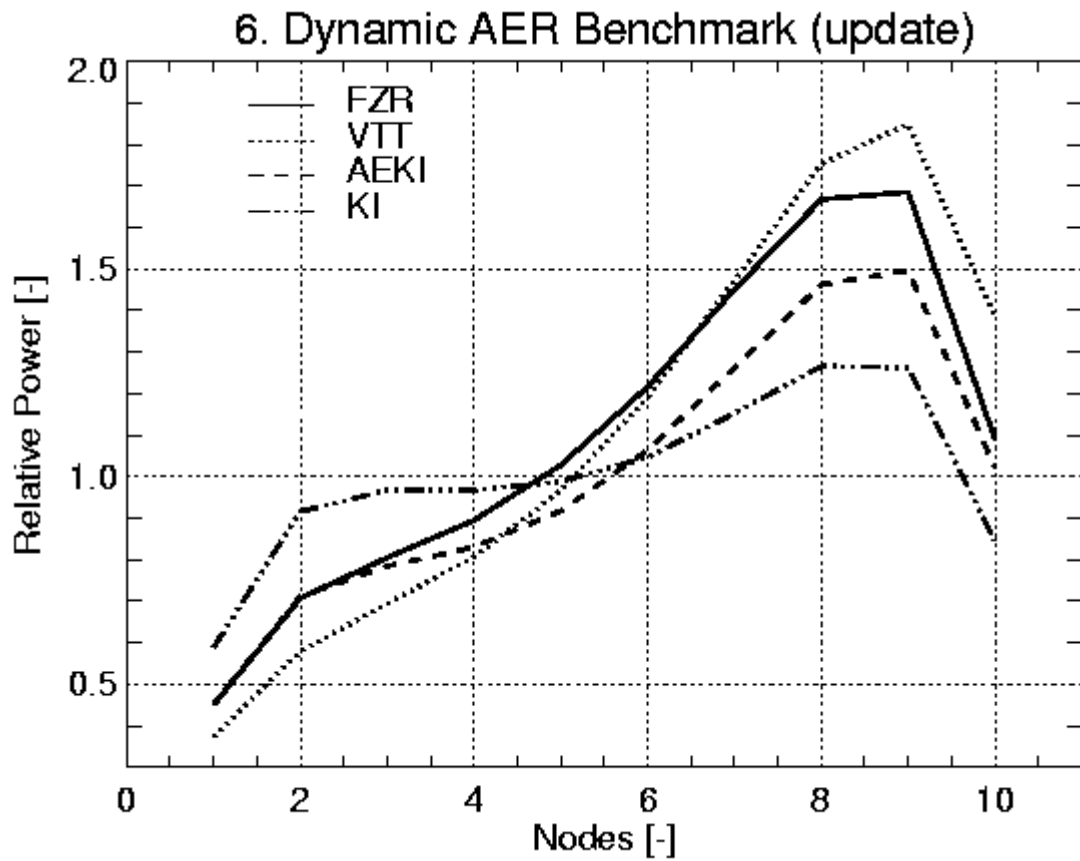


Fig. 38 Axial power distribution at the time of second power maximum

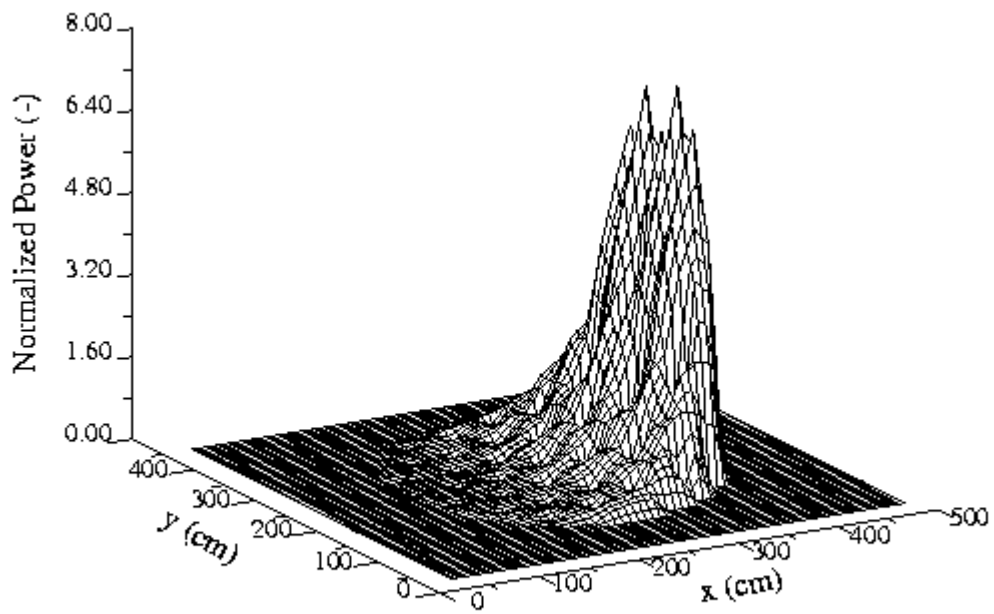


Fig. 39 Normalized 2D power distribution at the moment of second power maximum (FZR)

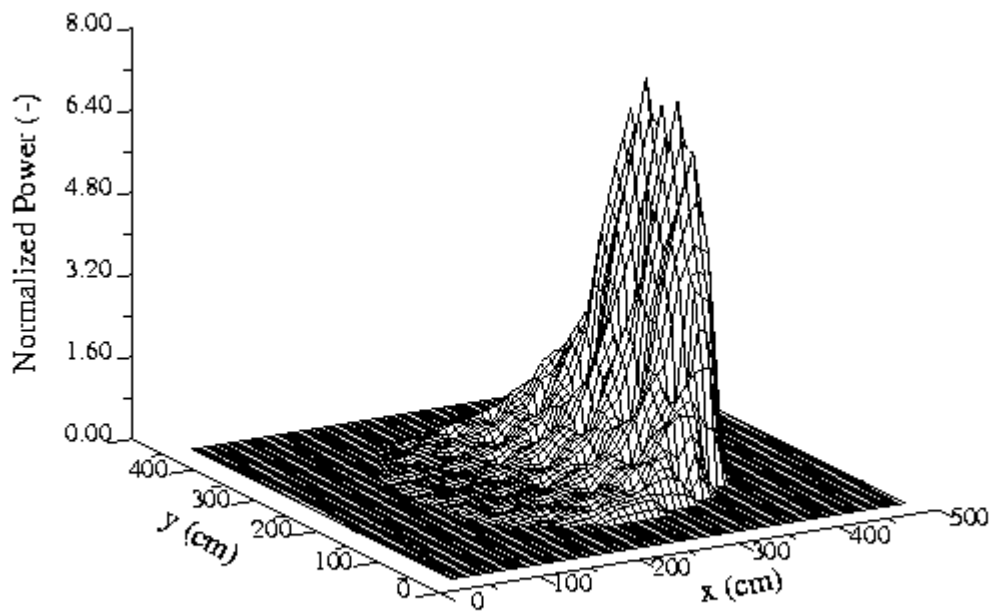


Fig. 40 Normalized 2D power distribution at the moment of second power maximum (VTT)

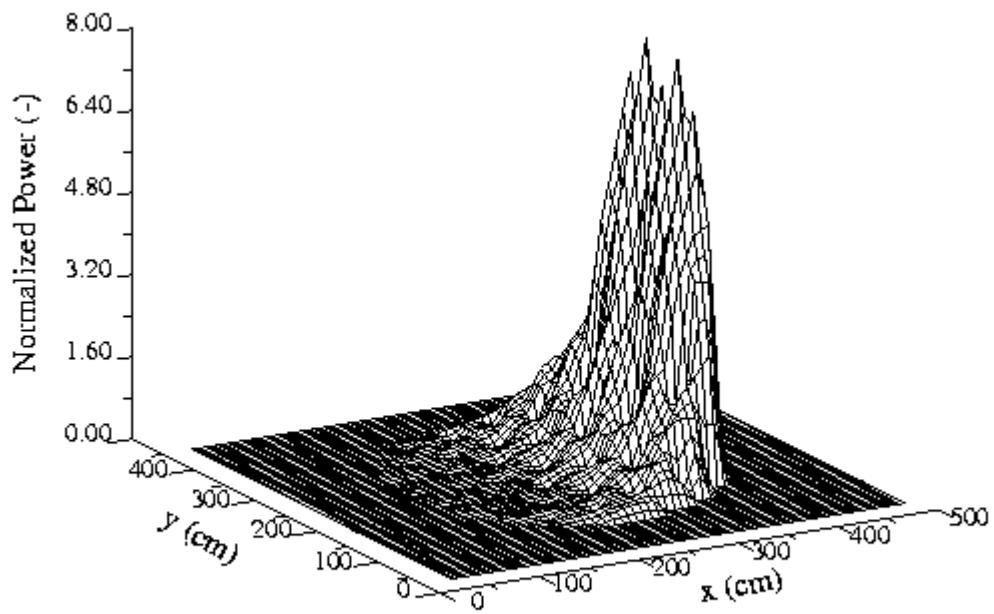


Fig. 41 Normalized 2D power distribution at the moment of second power maximum (AEKI)

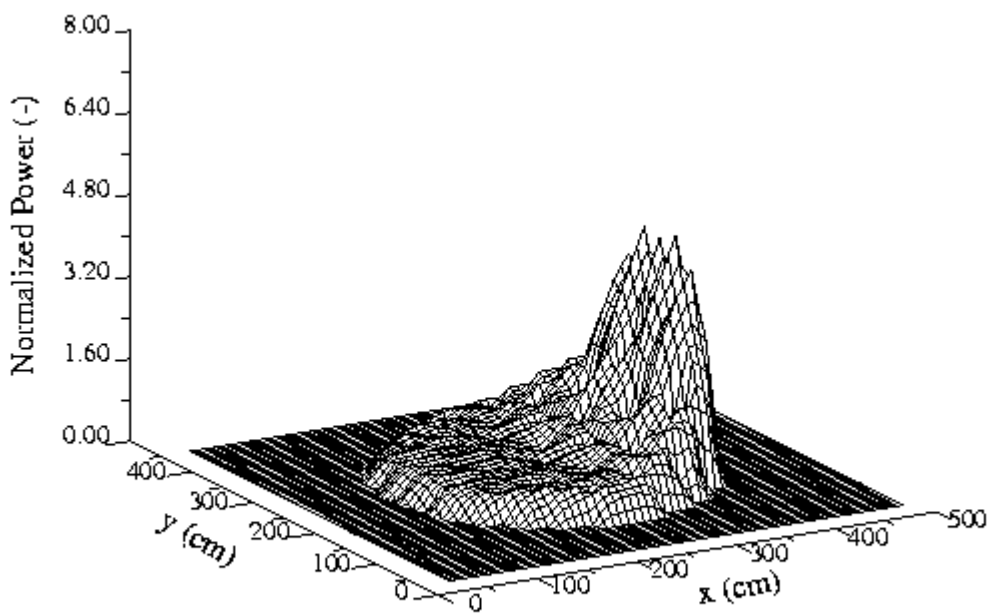


Fig. 42 Normalized 2D power distribution at the moment of second power maximum (KI)

### 6. Dynamic AER Benchmark (update)

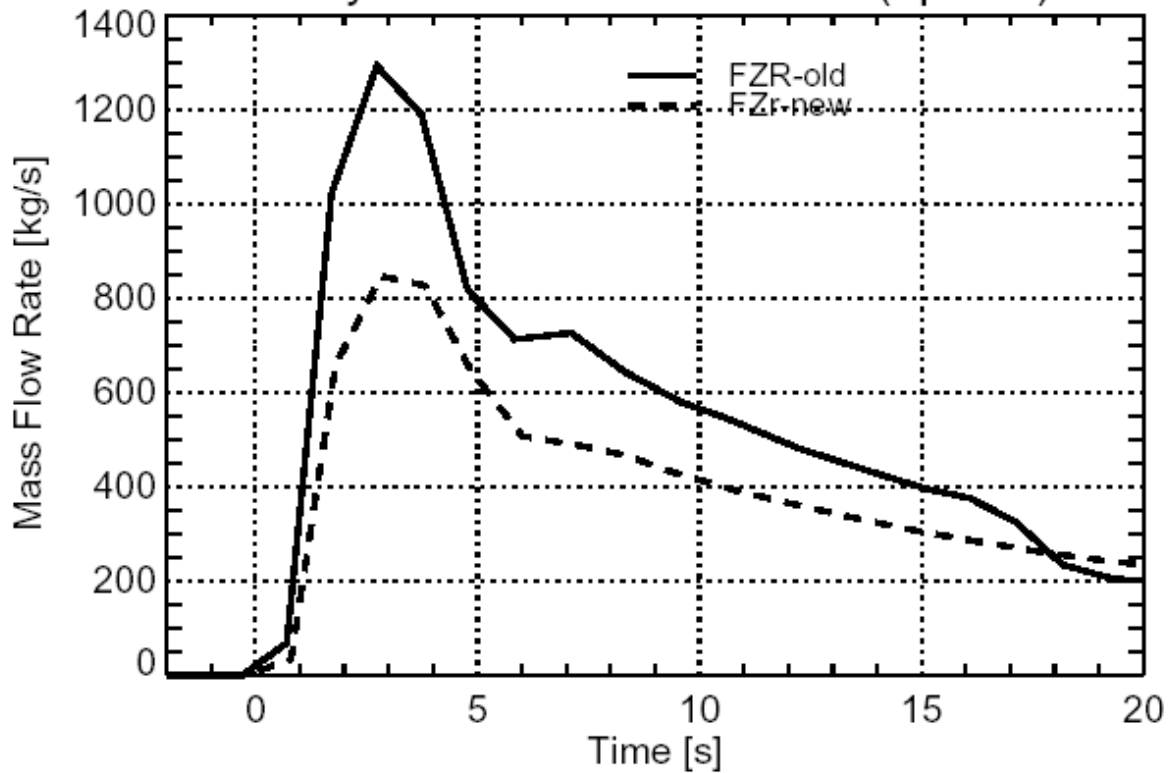


Fig. 43 Leak mass flow rate in the FZR-calculations

### 6. Dynamic AER Benchmark (update)

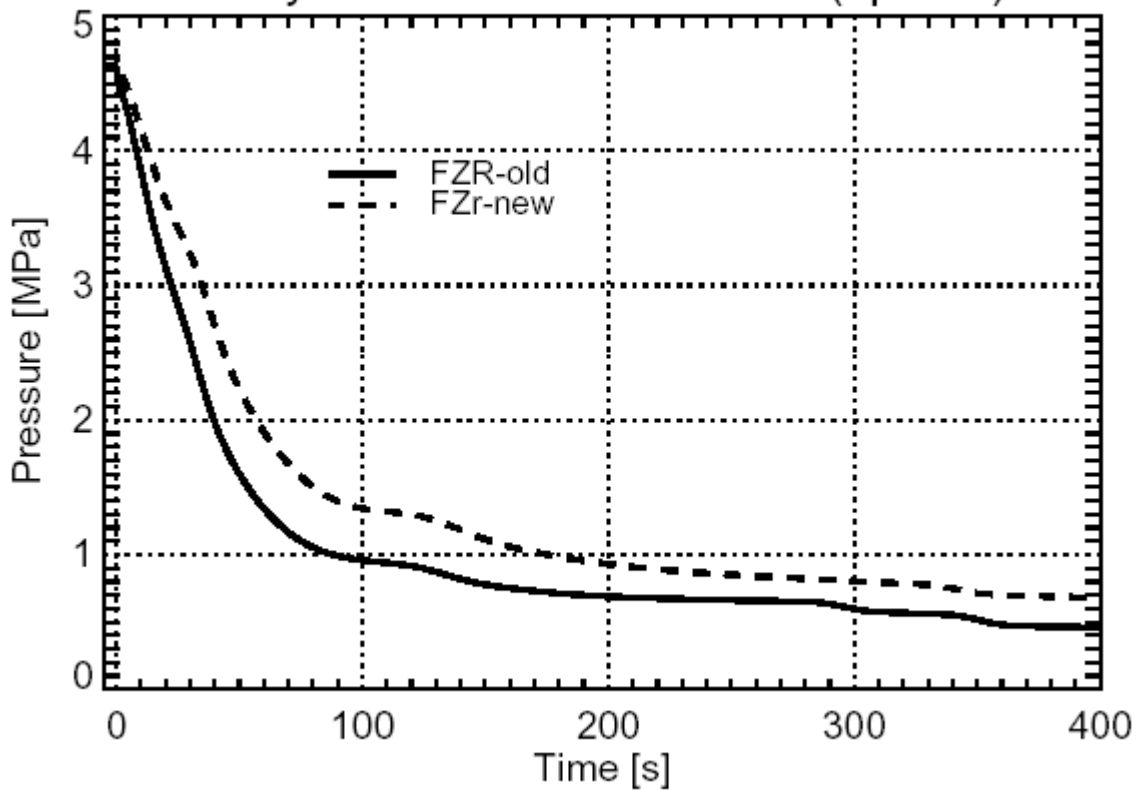


Fig. 44 Pressure behaviour in the broken steam generator in the FZR-calculations

### 6. Dynamic AER Benchmark (update)

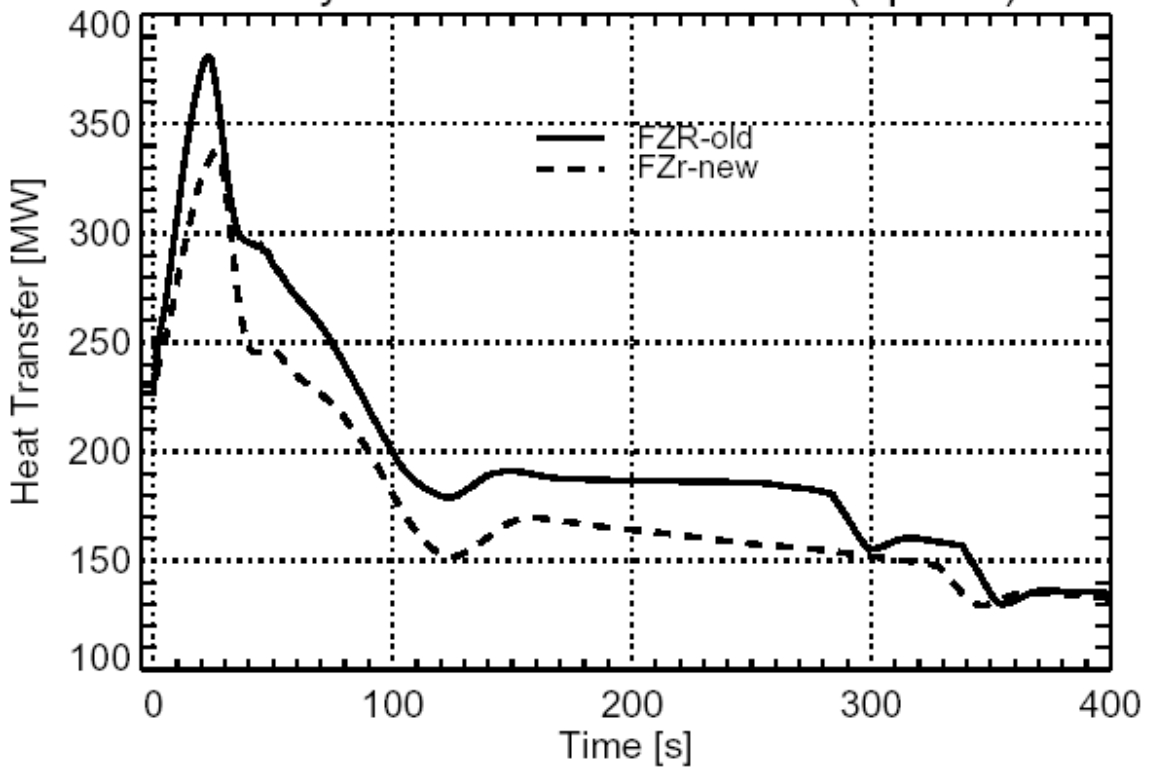


Fig. 45 Heat transfer in the broken steam generator in the FZR-calculations

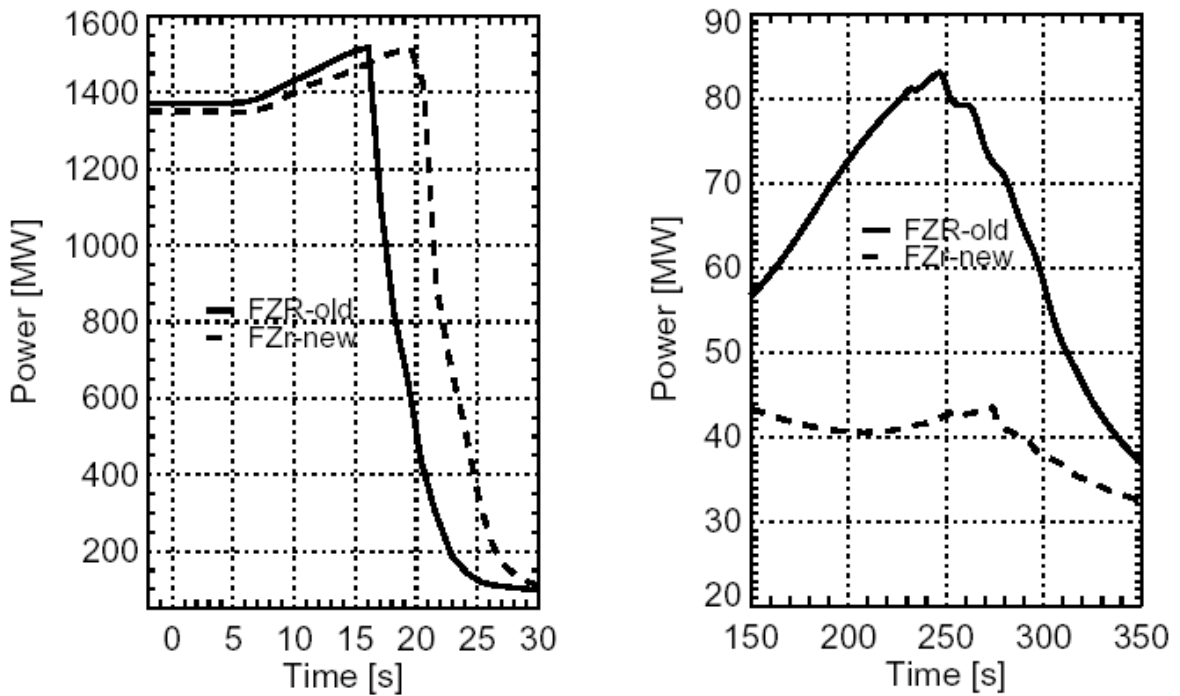


Fig. 46 Power behaviour in the FZR-calculations

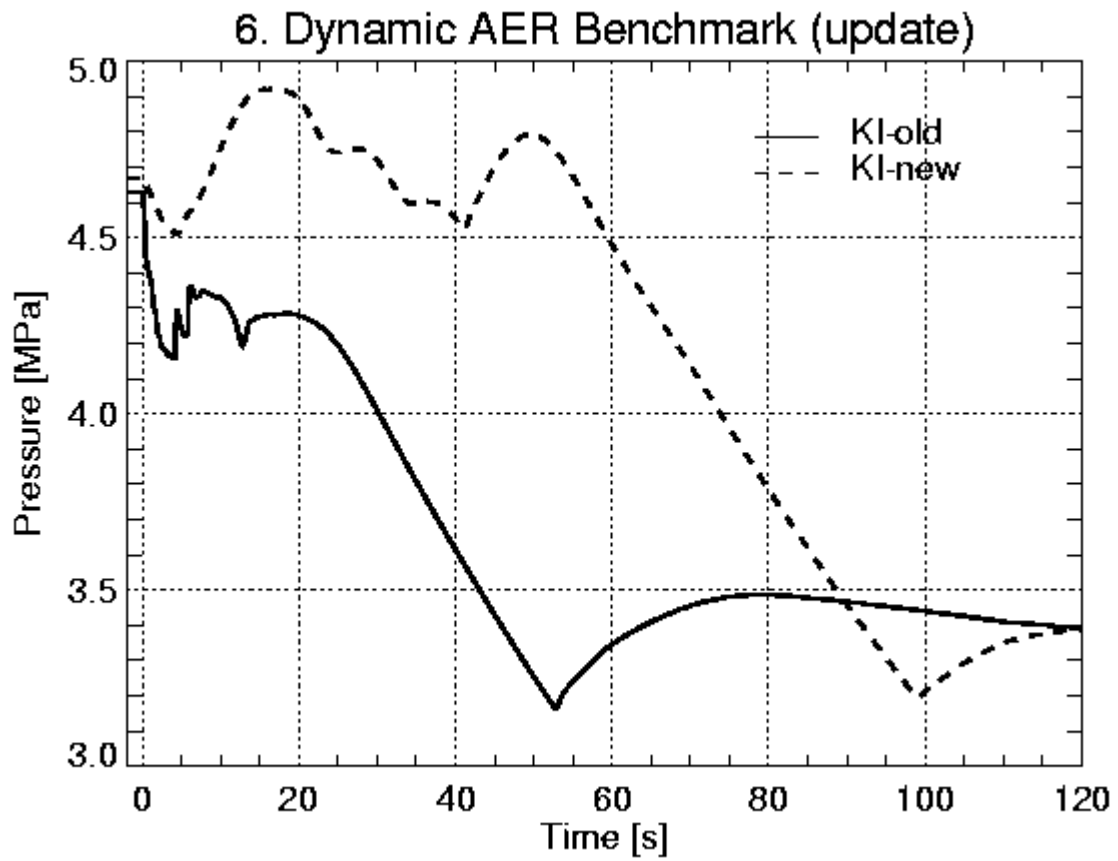


Fig. 47 Pressure in the intact steam generators in the KI-calculations

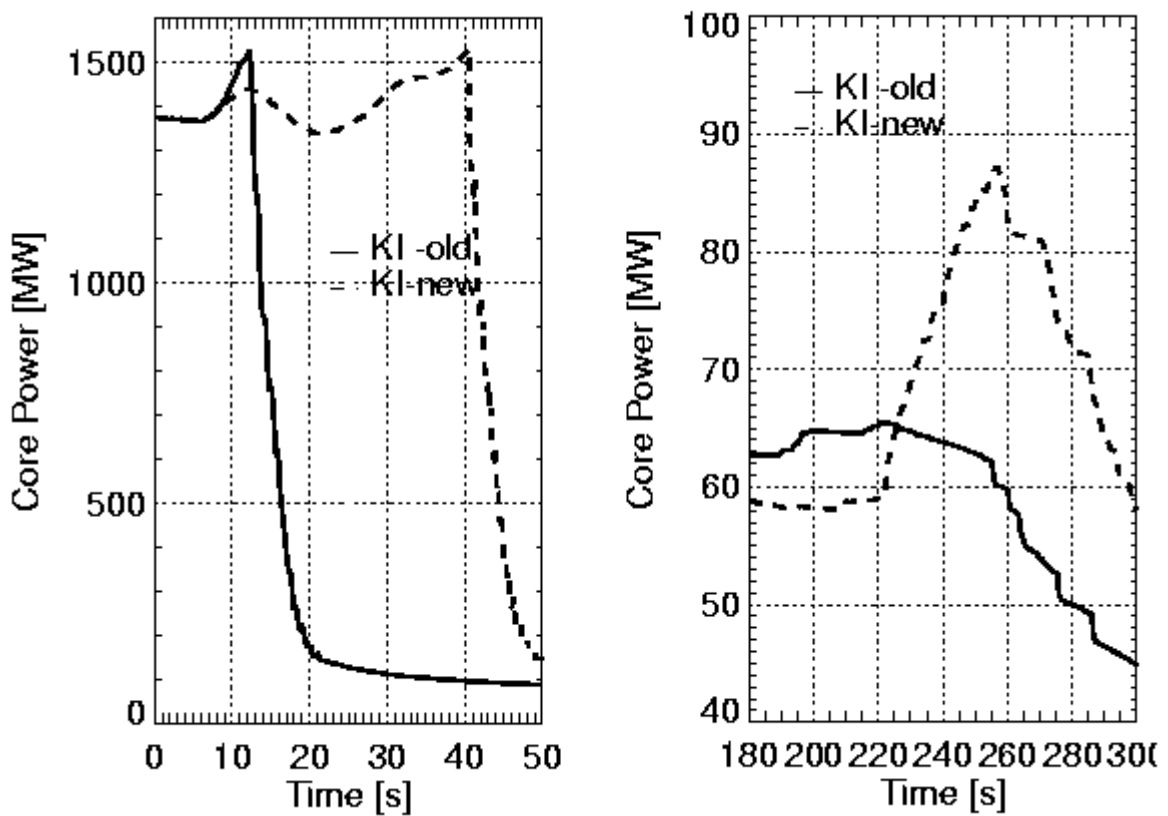


Fig. 48 Power behaviour in the KI-calculations